

Exploiting many-body localization for scalable variational quantum simulation

Chenfeng Cao,^{1,*} Yeqing Zhou,² Swamit Tannu,³ Nic Shannon,⁴ and Robert Joynt²

¹*Department of Physics, Hong Kong University of Science and Technology,
Clear Water Bay, Kowloon, Hong Kong, China*

²*Department of Physics, University of Wisconsin-Madison, Madison, WI 53706, USA*

³*Department of Computer Science, University of Wisconsin-Madison, Madison, WI 53706, USA*

⁴*Theory of Quantum Matter Unit, Okinawa Institute of Science and
Technology Graduate University, Onna-son, Okinawa 904-0412, Japan*

(Dated: May 21, 2024)

Variational quantum algorithms have emerged as a promising approach to achieving practical quantum advantages using near-term quantum devices. Despite their potential, the scalability of these algorithms poses a significant challenge. This is largely attributed to the “barren plateau” phenomenon, which persists even in the absence of noise. In this work, we explore the many-body localization (MBL)-thermalization phase transitions within a framework of Floquet-initialized variational quantum circuits and investigate how MBL could be used to avoid barren plateaus. The phase transitions are observed through calculations of the inverse participation ratio, the entanglement entropy, and a metric termed low-weight stabilizer Rényi entropy. By initializing the circuit in the MBL phase and employing an easily preparable initial state, we find it is possible to prevent the formation of a unitary 2-design, resulting in an output state with entanglement that follows an area- rather than a volume-law, and which circumvents barren plateaus throughout the optimization. Utilizing this methodology, we successfully determine the ground states of various model Hamiltonians across different phases and show that the resources required for the optimization are significantly reduced. We have further validated the MBL approach through experiments carried out on the 127-qubit *ibm_brisbane* quantum processor. These experiments confirm that the gradients needed to carry out variational calculations are restored in the MBL phase of a Heisenberg model subject to random unitary “kicks”. These results provide new insights into the interplay between MBL and quantum computing, and suggest that the role of MBL states should be considered in the design of quantum algorithms.

I. INTRODUCTION

Quantum computing holds the potential to revolutionize various scientific fields, including cryptography, optimization, quantum chemistry, and quantum simulation, by solving problems that are intractable for classical computers. One of the most promising techniques to harness this power in the near term is quantum variational optimization, which utilizes hybrid classical-quantum algorithms to efficiently optimize quantum circuits [1–3]. However, scaling these algorithms introduces several challenges, notably the so-called *barren plateau* phenomenon, in which the energy gradients needed for optimization become exponentially small [4–8].

Variational quantum algorithms (VQAs) represent a class of hybrid quantum-classical algorithms that capitalize on the strengths of both quantum and classical computing to address complex computational problems [2]. The fundamental concept behind VQAs involves parametrizing a quantum circuit and optimizing these parameters using classical methods. This strategy enables researchers to identify optimal or near-optimal solutions to specific problems while partially circumventing the limitations of current quantum hardware, such as restricted qubit coherence times and connectivities. A

typical VQA comprises two main components: a variational quantum circuit that produces the quantum state of interest, and a classical optimization routine that refines the parameters of the circuit to minimize a chosen cost function. Typical examples of VQAs include the variational quantum eigensolver [9, 10] for estimating the ground state energy of molecular systems and the quantum approximate optimization algorithm [11, 12] for solving combinatorial optimization problems.

While entanglement is an essential resource for quantum computation, excessive entanglement can be detrimental. In measurement-based quantum computing, this excessive entanglement results in inefficient “CQ-universality” [13], and in VQAs, it leads to barren plateaus [5], characterized by exponentially decaying gradients within the optimization landscape. This decay significantly complicates the process of locating optimal solutions. The barren plateau phenomenon is intricately linked to the entanglement characteristics of the output states in these circuits, where the formation of a unitary 2-design causes high entanglement and leads to gradient decay. Therefore, controlling entanglement is crucial for the effective implementation of large-scale VQAs.

The barren plateau phenomenon presents a substantial obstacle to scaling VQAs by rendering gradient-based optimizers inefficient, especially within high-dimensional parameter spaces. Over recent years, researchers have explored a variety of strategies to mitigate this issue. These include employing local cost functions and (lo-

* chenfeng.cao@connect.ust.hk

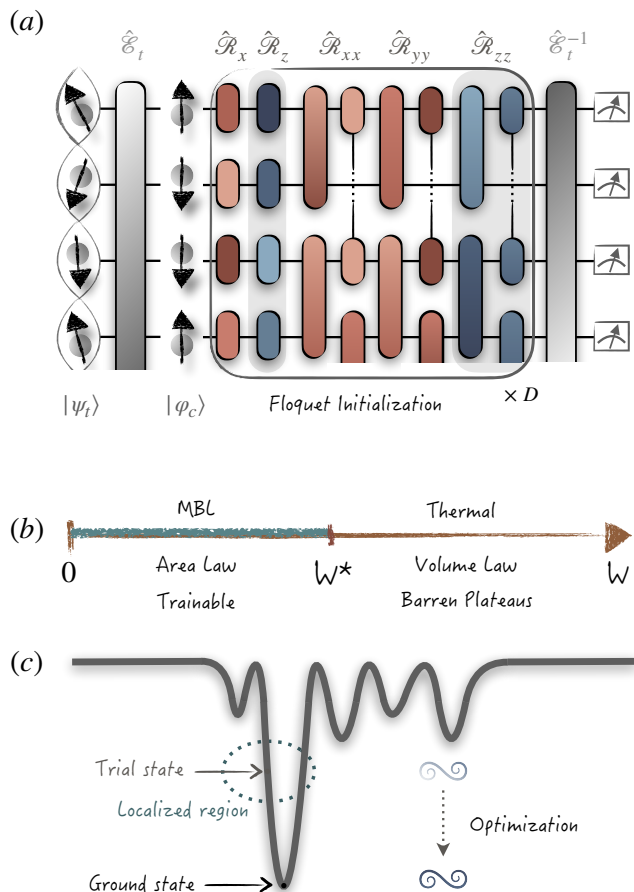


Figure 1. Schematic representation of the Floquet-initialized variational quantum circuit, the localization-thermalization phase transition, and the optimization landscape. (a) Diagram of a variational quantum circuit. The illustration includes four qubits as a segment of a larger circuit, resulting in some 2-qubit gates acting on adjacent pairs $Q_i - Q_j$ appearing truncated. The circuit begins with a low-entanglement trial state. Steady rotation angles within $\hat{\mathcal{R}}_z$ and $\hat{\mathcal{R}}_{zz}$ are initialized randomly within $[-\pi, \pi)$, while the kick rotation angles in $\hat{\mathcal{R}}_x$, $\hat{\mathcal{R}}_{xx}$, and $\hat{\mathcal{R}}_{yy}$ are initialized within $[-W, W]$. (b) Transition of the variational quantum circuit between the many-body localized (MBL) phase and the thermal phase as a function of the kick strength W . Below a critical threshold W^* , the circuit remains in the MBL phase, characterized by output state entanglement entropy adhering to the area law and trainable circuit parameters. Above W^* , the circuit enters the thermal phase, where the output state’s entanglement entropy follows the volume law, rendering the circuit parameters untrainable. (c) Depiction of the optimization landscape for an MBL-initialized circuit. The initial output state is localized to a trial state, ideally positioned in the same “gorge” as the ground state, facilitating effective optimization.

cally) shallow circuits [14, 15], utilizing iterative search schemes [16], and adopting problem-specific *Ansätze* [17, 18]. Furthermore, several effective approaches have been developed to reduce circuit entanglement, such as meta-learning for low-entanglement circuit initializations [19], implementing successive shadow tomography throughout

the optimization process [20], and incorporating intermediate projective measurements [21]. Additionally, the relationship between an *Ansatz*’s expressibility and its gradient magnitudes has been identified as a critical factor in overcoming barren plateaus [22], showing that highly expressive *Ansätze* typically exhibit flatter cost landscapes, complicating their trainability.

In this study, we employ the concept of *many-body localization* (MBL), a phenomenon extensively analyzed within the field of condensed matter physics, to address the challenges posed by barren plateaus in VQAs. MBL occurs in disordered quantum systems and is characterized by a transition from a thermalized phase to a localized phase as the disorder intensity increases [23–27]. In the thermalized phase, a quantum system reaches thermal equilibrium with entanglement entropy that scales with the system’s volume [28]. Conversely, in the MBL phase, the system exhibits area-law scaling of entanglement entropy, indicative of localization without thermalization. The MBL transition has attracted considerable attention in recent years, as it highlights the interplay between disorder, interactions, and quantum entanglement in strongly correlated quantum systems.

Further investigation into MBL has revealed several important phenomena relevant to quantum information science, such as the emergence of local integrals of motion and enhanced resilience of quantum information against decoherence in MBL systems [26]. These properties have inspired a plethora of research into the interaction between MBL and quantum computing, including studies on accelerating quantum annealing through many-body delocalization terms [29], probing MBL with the variational quantum eigensolver [30], analyzing the correlation between MBL and the expressibility (trainability) of analog systems [31], and Floquet phases of Trotterized quantum circuits [32, 33]. Moreover, recent experimental work has demonstrated the extraction of local integrals of motion within the MBL phase using a programmable quantum computer [34].

Here we continue along this road and explore the MBL transition within the context of variational quantum optimization and propose an MBL-based protocol to suppress excessive entanglement and mitigate barren plateaus. Our approach is inspired by the dynamics of MBL in Floquet systems [35–37], which are characterized by a time-dependent Hamiltonian that periodically repeats. These systems exhibit a rich variety of dynamical behaviors, including an MBL-delocalization transition at specific driving frequencies [35, 36]. We leverage the structural similarities between these periodically driven systems and bricklayer quantum circuits to develop a Floquet-initialized variational quantum circuit for quantum optimization, which similarly exhibits an MBL-delocalization transition. The circuits utilized in our study are not only hardware-efficient but also universal. In the MBL phase, the entanglement entropy follows an area law, whereas in the thermal phase, it adheres to a volume law. Importantly, the robustness of

the cost gradient in the MBL phase effectively precludes the emergence of barren plateaus. Our protocol begins with a weakly entangled initial trial state of relatively low energy and initiates the circuit in the MBL phase to minimize initial expressibility. During the optimization process, the circuit’s expressibility remains unrestricted; however, despite deviations from the strict Floquet setup, the circuit effectively avoids evolving into a unitary 2-design. This behavior suggests that the optimization trajectories are generally free from barren plateaus when initiated properly. Numerical results confirm that our protocol significantly enhances optimization times for target system Hamiltonians across various phases.

To validate the effectiveness of our protocol, we introduce new analytical tools. First, we establish a mathematical relationship between quantum t -designs and a standard measure of MBL, the inverse participation ratio (Theorem 1). Second, we introduce a novel metric, the low-weight stabilizer Rényi entropy $M_{t,k}$, which is not only efficient to calculate but also correlates with t -designs (Theorem 2). These tools facilitate a deeper understanding of t -designs and clarify the link between MBL and efficient quantum optimization., thereby elucidating the connection between MBL and efficient quantum optimization. The theoretical absence of barren plateaus within the MBL phase is further supported under plausible assumptions (Observation 1, Theorem 3).

We also present an explicit experimental validation of the MBL approach, based on circuits with up to 31 qubits, run on the *ibm_brisbane* quantum processor. These experiments confirm that the gradients needed for variational optimization are restored within the MBL phase of the Heisenberg model subject to random unitary “kicks”.

The remainder of this paper is organized as follows: In Section II, we detail the configuration of our Floquet-initialized circuits, including various connectivities and the initialization scheme. Section III examines the MBL-delocalization transition from the perspectives of the relative inverse participation ratio, entanglement entropy, and low-weight stabilizer Rényi entropy. In Section IV, we discuss the trainability transition of the circuit and apply our protocol numerically to the Aubry-André model across different phases. Section V presents experimental results obtained on the *ibm_brisbane* quantum processor. Finally, Section VI concludes with a summary of our findings and outlines potential future research directions in MBL and quantum computing.

II. METHODOLOGY

In this study, we utilize an n -qubit brick-layer hardware-efficient variational quantum circuit that incorporates Pauli- X , $-Y$, $-XX$, $-YY$, and $-ZZ$ rotation gates, as depicted in Fig. 1 (a). Unlike the *Hamiltonian variational Ansatz* [10, 17], this variational *Ansatz* is capa-

ble of realizing arbitrary unitary evolution with sufficient depth and adequate optimization, which should enable broad applications in quantum information processing.

Before executing the variational quantum circuit, we establish a low-entanglement trial state, $|\psi_t\rangle$, using classical mean-field methods like the Hartree-Fock method [38, 39] or matrix product states [40, 41]. This state, which is efficiently preparable from a computational basis state such as $|\varphi_c\rangle = |\uparrow\rangle|\uparrow\rangle|\downarrow\rangle\dots|\uparrow\rangle$ through a low-resource invertible quantum channel $\hat{\mathcal{E}}_t$, is anticipated to capture crucial information about the target ground state’s entanglement structure.

The state $|\varphi_c\rangle$ is processed through a variational quantum circuit configured with Floquet-initialized parameters:

$$\hat{U}(\boldsymbol{\theta}) = \prod_{l=1}^D \left(\prod_{\substack{\alpha \in \\ \{x,y,z\}}} \hat{\mathcal{R}}_{\alpha\alpha}(\boldsymbol{\theta}_{\alpha\alpha}^{(l)}) \right) \left(\prod_{\alpha \in \{x,z\}} \hat{\mathcal{R}}_{\alpha}(\boldsymbol{\theta}_{\alpha}^{(l)}) \right). \quad (1)$$

Here, D denotes the circuit’s depth, quantified by the number of its layers. For Pauli index $\alpha \in \{x, y, z\}$, we define:

$$\hat{\mathcal{R}}_{\alpha}(\boldsymbol{\theta}_{\alpha}^{(l)}) = \prod_{j=1}^n \exp\left(-i\frac{\theta_{\alpha}^{(lj)}}{2}\hat{\sigma}_j^{\alpha}\right) \quad (2)$$

$$\hat{\mathcal{R}}_{\alpha\alpha}(\boldsymbol{\theta}_{\alpha\alpha}^{(l)}) = \prod_{\substack{(j,k) \in \\ \text{edges}(G)}} \exp\left(-i\frac{\theta_{\alpha\alpha}^{(ljk)}}{2}\hat{\sigma}_j^{\alpha}\hat{\sigma}_k^{\alpha}\right), \quad (3)$$

where $\boldsymbol{\theta}_{\alpha}^{(l)}$ denotes the rotation angles for single-qubit α -Pauli rotations in the l -th layer, and $\boldsymbol{\theta}_{\alpha\alpha}^{(l)}$ pertains to two-qubit α -Pauli rotations in the same layer. G denotes the connectivity graph of the qubits, specifying which qubits are linked by two-qubit gates.

The Floquet initialization strategy involves first uniformly sampling the first-layer *steady parameters* $\theta_z^{(1j)}$ and $\theta_{zz}^{(1jk)}$ from the interval $[-\pi, \pi)$, and the *kick parameters* $\theta_x^{(1j)}$, $\theta_{xx}^{(1jk)}$, $\theta_{yy}^{(1jk)}$ from $[-W, W]$, where W indicates the *kick strength*. These parameters are consistently replicated across all layers $l = 1, 2, \dots, D$:

$$\boldsymbol{\theta}_{\alpha}^{(l)} = \boldsymbol{\theta}_{\alpha}^{(l')} \quad \forall l, l' \in \{1, 2, \dots, D\}, \quad (4)$$

$$\boldsymbol{\theta}_{\alpha\alpha}^{(l)} = \boldsymbol{\theta}_{\alpha\alpha}^{(l')} \quad \forall l, l' \in \{1, 2, \dots, D\}, \quad (5)$$

creating a periodically repetitive initial parameter set, denoted as $\Theta_{\text{prd}}(W)$. Denoting the unitary channel of the l -th layer as \hat{U}_l , the whole *Ansatz* fundamentally applies the $|\psi_t\rangle$ -dependent transformations $\hat{\mathcal{E}}_t^{-1} \circ \hat{U}_l \circ \hat{\mathcal{E}}_t$ sequentially on the trial state. From the expressibility perspective [6, 22], the expressibility of each circuit layer in our configuration does not cumulatively amplify to the D -th power due to the Floquet replication, thereby effectively circumventing the exponential trend towards the Haar distribution.

Upon executing $\hat{U}(\boldsymbol{\theta}_{\text{init}})$ with initial parameters $\boldsymbol{\theta}_{\text{init}} \in \Theta_{\text{prd}}(W)$ and applying the inverse trial channel $\hat{\mathcal{E}}_t^{-1}$, the initial output state,

$$|\psi(\boldsymbol{\theta}_{\text{init}})\rangle = \hat{\mathcal{E}}_t^{-1} \circ \hat{U}_1^D \circ \mathcal{E}_t(|\psi_t\rangle\langle\psi_t|), \quad (6)$$

is localized near the trial state $|\psi_t\rangle$, provided the kick strength is maintained below a certain threshold to ensure initialization within an MBL phase. This localization generates significant initial gradients, facilitating effective subsequent optimization. During the optimization stage, rotation angles in different layers are individually updated to better minimize the output energy. With sufficient depth and properly adjusted parameters, the variational quantum circuit is capable of preparing the exact ground state, as this *Ansatz* is universal, able to approximate any unitary transformation with arbitrary precision given an adequate number of qubits and circuit layers. A detailed proof of this universality is presented in Appendix A. While the output state is not confined to the vicinity of $|\psi_t\rangle$ during optimization—indicating a release from MBL constraints—numerical evidence in Sec. IV suggests that MBL-based initialization likely prevents the system from evolving into a random 2-design state, providing optimization trajectories free from barren plateaus. For subsequent discussions, $\hat{\mathcal{E}}_t(\rho)$ is considered a low-depth unitary circuit, expressed as $\hat{\mathcal{E}}_t(\rho) = \hat{U}_t \rho \hat{U}_t^\dagger$.

III. MBL-THERMALIZATION TRANSITION

Many-body localization (MBL) arises in disordered quantum systems with interacting constituents, where disorder can trigger a transition from ergodic to non-ergodic behavior, preventing the system from reaching thermal equilibrium [23–26]. As a result, the initial information is preserved. In this section, we analyze the MBL-thermalization phase transition in our setup using three metrics: the inverse participation ratio, the entanglement entropy, and the low-weight stabilizer Rényi entropy.

Initially, we delineate the concept of quantum t -designs, critical for analyzing random quantum states and channels [42–44]. An ensemble of parameterized unitary operations $\hat{U}(\boldsymbol{\theta})$, with $\boldsymbol{\theta}$ uniformly sampled from the parameter space Θ , forms a t -design if and only if it satisfies

$$\int_{\Theta} (\hat{U}(\boldsymbol{\theta}) \otimes \hat{U}(\boldsymbol{\theta})^\dagger)^{\otimes t} d\boldsymbol{\theta} = \int_{\mathcal{U}} (\hat{U} \otimes \hat{U}^\dagger)^{\otimes t} d\mu_H(\hat{U}), \quad (7)$$

where \mathcal{U} represents the space of unitary matrices, and $d\mu_H(\hat{U})$ denotes the Haar measure.

Within the context of variational quantum optimization, it has been shown that when the variational quantum circuit ensemble forms a unitary 2-design, the gradients decay exponentially regardless of the locality of the cost function [4, 14].

Inverse Participation Ratio—The inverse participation ratio (IPR) is a valuable metric for characterizing the localization properties of quantum states. For an n -qubit state $|\psi\rangle$, the t -th-order-moment IPR with respect to the basis states $\{|\beta_j\rangle\}$ is defined as

$$\text{IPR}_t(|\psi\rangle) = \sum_j |\langle\beta_j|\psi\rangle|^{2t}. \quad (8)$$

A higher IPR_t value indicates a more localized state, while a lower value indicates greater delocalization. As t increases, the IPR becomes increasingly sensitive to localization properties. In MBL studies, IPR_2 is commonly used to differentiate between localized and delocalized eigenstates [45, 46]. Here, we select basis states $\{|\beta_j\rangle = \hat{U}_t^\dagger|j\rangle\}$ with $\{|j\rangle\}_{j=1,2,\dots,2^n}$ representing the computational basis. The trial state $|\psi_t\rangle$ belongs to $\{|\beta_j\rangle\}$. The IPR_t measures how well the output state is localized to the trial state, noting that IPR's definition is basis-dependent.

There is a profound link between the inverse participation ratio and the t -design characteristic:

Theorem 1 *Given that $\{\hat{U}(\boldsymbol{\theta})\}$, with $\boldsymbol{\theta}$ uniformly sampled from Θ , forms a unitary t -design. For any arbitrary n -qubit input state $|\psi_{\text{in}}\rangle$, the expected inverse participation ratio of the output state $|\psi(\boldsymbol{\theta})\rangle = \hat{U}(\boldsymbol{\theta})|\psi_{\text{in}}\rangle$ with respect to some basis states $\{|\beta_j\rangle\}$ satisfies*

$$\int_{\Theta} \text{IPR}_t(|\psi(\boldsymbol{\theta})\rangle) d\boldsymbol{\theta} = \frac{2^n t!}{(t + 2^n - 1)!}. \quad (9)$$

For $t = 2$, specifically:

$$\int_{\Theta} \text{IPR}_2(|\psi(\boldsymbol{\theta})\rangle) d\boldsymbol{\theta} = \frac{2}{2^n + 1}. \quad (10)$$

A proof is available in Appendix B.

This result indicates that the inverse participation ratio not only quantifies localization but also determines whether an ensemble of unitaries violates the unitary t -design. However, unlike the frame potential defined in Refs. [42, 47], IPR_t is not suitable for quantifying the deviation of $\{|\psi(\boldsymbol{\theta})\rangle\}$ from t -design with $t \geq 2$, as the basis states $\{|\beta_j\rangle\}$ do not form a state 2-design. Instead, when $t \geq 2$, the dimension of the subspace spanned by the t -fold basis states is considerably smaller than the dimension of the t -fold symmetric subspace $\vee^t \mathbb{C}^{2^n}$ [48], denoted by $d_{\text{sym}}^{(t)}$.

$$\dim(\text{Span}\{|j\rangle^{\otimes t}\}) = 2^n \ll d_{\text{sym}}^{(t)} = \binom{t + 2^n - 1}{t}. \quad (11)$$

Despite these dimensional differences, we confirm that the output state ensemble qualifies as a state 2-design. This confirmation comes from our direct calculations of frame potentials, detailed in Appendix C. Additionally, we explore the expressibility of the Floquet initialization

for both the MBL and thermal phases in the same appendix, providing insights into the dynamic behaviors of these phases.

Entanglement Entropy—A pivotal characteristic of MBL is the behavior of the entanglement entropy (S_L) of a subsystem L :

$$S_L = -\text{Tr}(\rho_L \log \rho_L) \quad (12)$$

where ρ_L is the reduced density matrix for subsystem L . In thermalized systems, S_L adheres to a volume law scaling, proportional to subsystem size: $S_L \sim |L|^d$, where d denotes the spatial dimension of the system. In contrast, MBL systems exhibit an area law scaling, in which S_L increases proportionally to the boundary of the subsystem L : $S_L \sim |L|^{d-1}$ [28]. For one-dimensional systems, where $d = 1$, S_L essentially remains constant. The transition from volume law to area law scaling is a defining characteristic of MBL systems and has been extensively studied through numerical simulations [46, 49].

Low-Weight Stabilizer Rényi Entropy—The final metric we employ is a refined version of the stabilizer Rényi entropy, as defined in Ref. [50], which aims to quantify the magic resource (non-stabilizerness) of a quantum state. This metric provides valuable insights into quantum many-body systems, enhancing our understanding of complex patterns in ground-state wave functions [51] and the dynamics of quantum quenches [52]. Unlike the original definition, which encompasses all Pauli terms and is thus challenging to estimate in practical scenarios, our approach focuses solely on low-weight Pauli terms. We define the *low-weight stabilizer Rényi entropy* as follows:

Definition 1 Given an n -qubit state $|\psi\rangle$, we define its low-weight stabilizer Rényi entropy of order t and locality k as

$$M_{t,k}(|\psi\rangle) = (1-t)^{-1} \log \sum_{\hat{P} \in \mathcal{P}_{n,k}} \frac{\langle \psi | \hat{P} | \psi \rangle^{2t}}{\text{card}(\mathcal{P}_{n,k})}, \quad (13)$$

where $\mathcal{P}_{n,k}$ is the set of n -qubit Pauli strings with phase +1 and no more than k non-identity terms.

This metric characterizes the extent to which a quantum state $|\psi\rangle$ can be stabilized by some low-weight Pauli tensor products, a concept particularly relevant in quantum error correction contexts [53].

The primary benefit of utilizing $M_{t,k}$, compared to the standard stabilizer Rényi entropy or entanglement entropy, lies in its computational tractability; it requires only poly(n) expectation values when k is fixed, significantly simplifying calculations. This feature makes $M_{t,k}$ particularly valuable in scenarios where the observables of interest are predominantly low-weight Pauli terms. In contrast to the full stabilizer Rényi entropy, which assesses a state's deviation from t -designs across all possible Pauli strings, $M_{t,k}$ focuses on capturing this deviation specifically for local terms, aligning more closely

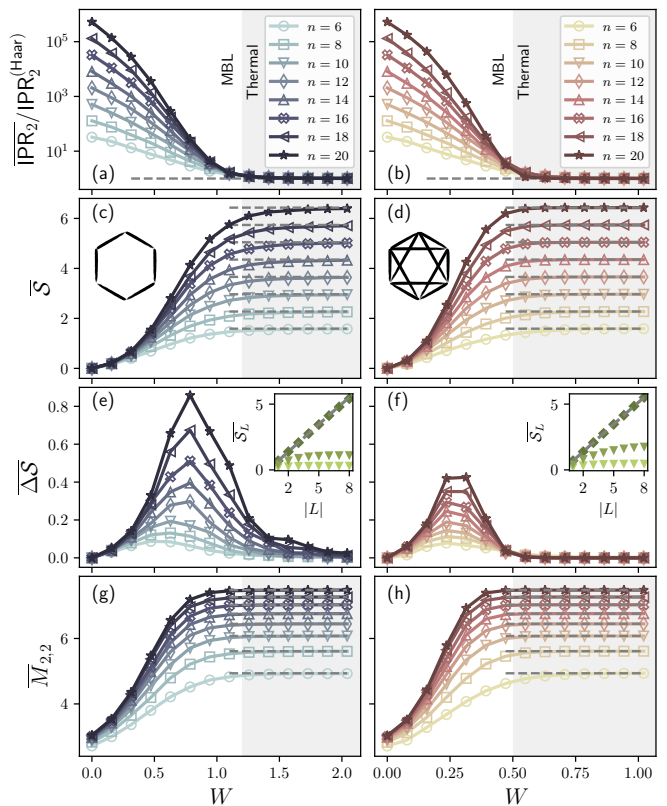


Figure 2. Characterization of the MBL-thermalization transition. Panels (a, c, e, g) represent results for the 1D ring topology, and panels (b, d, f, h) represent results for the $Ci_n(1,2)$ topology. (a, b) Ratios of the inverse participation ratio, IPR_2 [Eq. (10)], to the Haar-random inverse participation ratio, $\text{IPR}_2^{(\text{Haar})}$ [Eq. (17)], as a function of kick strength W . The grey dashed lines correspond to 1. (c, d) Half-chain entanglement entropy versus kick strength W . The grey dashed lines correspond to $S^{(\text{Page})}$ [Eq. (14)]. Insets: Demonstration of the topologies of a 6-qubit ring and a $Ci_6(1,2)$ graph. (e, f) Entanglement entropy fluctuations versus kick strength W . Insets: Entanglement entropy of a local region L versus the size of L for both MBL ($W = 1/5, 2/5$ for the 1D ring topology and $W = 1/10, 1/5$ for the $Ci_n(1,2)$ topology) and thermal ($W = 7/5$ for 1D ring and $W = 7/10$ for $Ci_n(1,2)$) phases in a 20-spin chain. Darker green markers indicate circuits with higher W . The grey dashed lines correspond to $S^{(\text{Page})}$. (g, h) The low-weight stabilizer Rényi entropy of order 2 and locality 2 [Eq. (13)] versus kick strength W . The grey dashed lines correspond to the lower bound $\tilde{M}_{2,2}^{(\text{Haar})}$ [Eq. (20)].

with the physical observables relevant in many practical quantum computing tasks. The relation between $M_{t,k}$ and t -designs can be elaborated in the subsequent theorem:

Theorem 2 Assuming that $\hat{U}(\theta)$, with θ uniformly sampled from Θ , forms a unitary t -design where t is an even integer, any arbitrary n -qubit input state $|\psi_{in}\rangle$ trans-

formed by these operations satisfies:

$$\int_{\Theta} \sum_{\hat{P} \in \mathcal{P}_{n,k}} \frac{\langle \psi(\boldsymbol{\theta}) | \hat{P} | \psi(\boldsymbol{\theta}) \rangle^{2t}}{\text{card}(\mathcal{P}_{n,k})} d\boldsymbol{\theta} \quad (14)$$

$$= \frac{\binom{2^n+t-1}{t} - \binom{2^{n-1}+t/2-1}{t/2}}{\text{card}(\mathcal{P}_{n,k}) \binom{2^n+t-1}{t}} + \frac{\binom{2^{n-1}+t/2-1}{t/2}}{\binom{2^n+t-1}{t}}.$$

Let this value be denoted by $T_{t,k}$. By Jensen's inequality, the expected low-weight stabilizer Rényi entropy of order t and locality k of $|\psi(\boldsymbol{\theta})\rangle$ satisfies:

$$\int_{\Theta} M_{t,k}(|\psi(\boldsymbol{\theta})\rangle) d\boldsymbol{\theta} \geq \frac{\log(T_{t,k})}{1-t}. \quad (15)$$

Thus, computing $M_{t,k}$ provides an upper bound for measuring the extent to which a t -design has been formed. We denote the right-hand side of Inequality (15) as $\tilde{M}_{t,k}^{(\text{Haar})}$. The proof for Theorem 2 is provided in Appendix D.

Characterizing MBL and Thermalization—Utilizing the inverse participation ratio, entanglement entropy, and the low-weight stabilizer Rényi entropy as metrics, we investigate the MBL-delocalization phase transition in a square circuit with equal depth D and width n , and varying kick strength W . These circuits have $\text{poly}(n)$ depth and typically exhibit barren plateaus when parameters are independently and randomly sampled [14]. Without loss of generality, the trial state is assumed to be a product state, drawn from the set

$$\left\{ |\psi_t\rangle = \bigotimes_{j=1}^n U_j^{(\text{Haar})} |\uparrow\rangle |\uparrow\rangle \dots |\uparrow\rangle \right\}, \quad (16)$$

where each $U_j^{(\text{Haar})}$ represents a single-qubit Haar-random unitary operation applied to qubit Q_j . \hat{U}_t transforms the trial state to the computational basis state with which it shares the highest fidelity. We explore two types of connectivities: 1D rings and circulant graphs $\text{Ci}_n(1, 2)$.

The results for average IPR_2 , half-chain entanglement entropy and its fluctuations, and $M_{2,2}$ are depicted in Fig. 2 with each point averaged over at least 200 samples. For both connectivity graphs, when the kick strength is below a certain threshold W^* ($W^* \approx 6/5$ for the 1D ring and $W^* \approx 1/2$ for $\text{Ci}_n(1, 2)$, though slightly varying across different metrics), the output state remains localized to the trial state:

$$\overline{\text{IPR}}_2 \gg \text{IPR}_2^{(\text{Haar})} = \frac{2}{2^n + 1}; \quad (17)$$

the average half-chain entanglement entropy, $\overline{S}(\frac{n}{2}, n)$, is significantly lower than the Page value for a random pure state, $S^{(\text{Page})}(\frac{n}{2}, n)$ [54, 55]:

$$\overline{S}(\frac{n}{2}, n) \ll S^{(\text{Page})}(\frac{n}{2}, n) = \sum_{j=n/2+1}^{n^2/4} \frac{1}{j} - \frac{n-2}{2n}; \quad (18)$$

the entanglement entropy fluctuation, $\overline{\Delta S}$, is substantial; and the output state can be stabilized by some low-weight Pauli stabilizers to a certain extent

$$\overline{M}_{2,2} \ll M_{2,2}^{(\text{Haar})} = \log(\text{card}(\mathcal{P}_{n,2})) - \frac{1}{\mathcal{O}(\exp(n))}. \quad (19)$$

$M_{2,2}^{(\text{Haar})}$ can be approximated by the lower bound

$$\tilde{M}_{2,2}^{(\text{Haar})} = \log(\text{card}(\mathcal{P}_{n,2})) - \log\left(\frac{\text{card}(\mathcal{P}_{n,2}) + 2^{2n} + 2^{n+2}}{2^{2n} + 2^{n+2} + 3}\right) \quad (20)$$

When W exceeds this threshold, IPR_2 converges to $2/(2^n + 1)$, \overline{S} approaches $S^{(\text{Page})}$, $\overline{\Delta S}$ is around 0, and $\overline{M}_{2,2}$ gets close to

$$\log(\text{card}(\mathcal{P}_{n,2})) = \log\left(\frac{9n^2}{2} + \frac{3n}{2} + 1\right). \quad (21)$$

Insets for a 20-qubit system illustrate that the entanglement entropy in the MBL phase (with $W = 1/5, 2/5$ for the 1D ring and $W = 1/10, 2/10$ for $\text{Ci}_n(1, 2)$) follows the area law, while entanglement entropy in the thermal phase adheres to the volume law. It is conjectured (and has been proven for 1D systems) that the entanglement of the ground states of gapped spin systems obeys the area law [28, 56]. When preparing these states with variational quantum optimization, it is reasonable to initialize the variational quantum circuits in the MBL phase to maintain consistency in entanglement entropy and, preferably, entanglement structure. The optimal choice of the kick strength W depends on the hardware topology, circuit depth, and the entanglement properties of the ground state of the target Hamiltonian. Though these numerical results primarily pertain to square circuits, local information remains well-preserved even in deeper circuits. Detailed illustrations are available in Appendix F.

IV. VARIATIONAL OPTIMIZATION

This section explores the efficacy of variational quantum optimization strategies for preparing the ground state of the Aubry-André model across its various phases [57]. The Aubry-André model, extensively studied in condensed matter physics, is known for its phase transition between Anderson localized and extended phases in the absence of particle-particle interactions, and between MBL and ergodic phases when particle-particle interactions are present. This transition is controlled by a single parameter. The model features a one-dimensional chain of particles, where each particle is subject to nearest-neighbor hopping and a quasiperiodic potential. The Hamiltonian in its spinless fermion

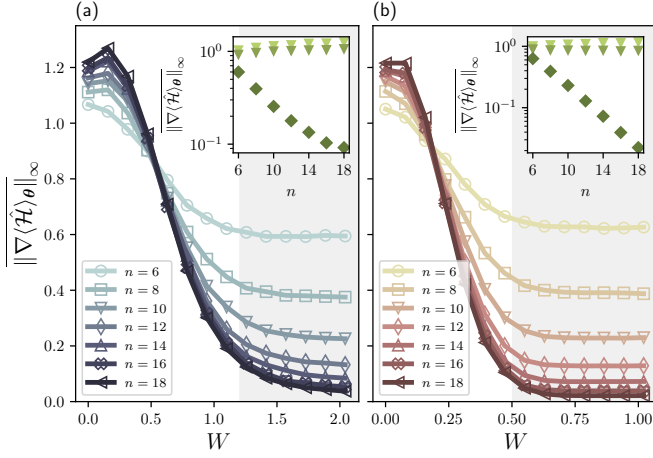


Figure 3. Visualization of the absence of barren plateaus in the MBL phase and their presence in the thermal phase after sampling the initial circuit parameters, analyzed using the target Hamiltonian $\hat{\mathcal{H}}_{AA}$ (defined in Eq. (23)). **(a)** Gradient norms plotted as a function of kick strength W for a 1D ring topology. **(b)** Gradient norms as a function of W for a $Ci_n(1,2)$ lattice topology. Insets illustrate the gradient scaling at various W values, emphasizing the contrast between the MBL phase (e.g., $W = 1/5, 2/5$ for the 1D ring and $W = 1/10, 1/5$ for the $Ci_n(1,2)$ topology) and the thermal phase (e.g., $W = 7/5$ for the 1D ring and $W = 7/10$ for the $Ci_n(1,2)$ topology). Darker green markers in the insets denote circuits with higher W .

representation is given by:

$$\begin{aligned} \hat{\mathcal{H}}_{AA}^{(fm)} = & -J \sum_j (\hat{c}_j^\dagger \hat{c}_{j+1} + \hat{c}_{j+1}^\dagger \hat{c}_j) + \Gamma \sum_j \hat{n}_j \hat{n}_{j+1} \\ & + V \sum_j \cos(2\pi\alpha j + \phi) \hat{n}_j \end{aligned} \quad (22)$$

Here, J denotes the hopping amplitude between adjacent sites, \hat{c}_j^\dagger (\hat{c}_j) represents the creation (annihilation) operator at site j , \hat{n}_j is the number operator at site j , Γ denotes the interaction strength between neighboring particles, V is the strength of the quasiperiodic potential, α is an irrational number determining the quasiperiodicity of the potential, and ϕ is a phase factor.

Utilizing the Jordan-Wigner transformation [58], the qubit form of the Aubry-André model is derived as:

$$\begin{aligned} \hat{\mathcal{H}}_{AA} = & -\frac{J}{2} \sum_j (\hat{\sigma}_j^x \hat{\sigma}_{j+1}^x + \hat{\sigma}_j^y \hat{\sigma}_{j+1}^y) + \frac{\Gamma}{4} \sum_j \hat{\sigma}_j^z \hat{\sigma}_{j+1}^z \\ & - \frac{V}{2} \sum_j (\cos(2\pi\alpha j + \phi) + \frac{\Gamma}{V}) \hat{\sigma}_j^z. \end{aligned} \quad (23)$$

In the absence of interactions ($\Gamma = 0$), the transition between Anderson localized and extended phases is contingent upon the relative magnitudes of the hopping amplitude J and the quasiperiodic potential strength V . The system resides in a localized phase when $|V| > 2|J|$, and

in an extended phase when $|V| < 2|J|$. The critical transition occurs at $|V| = 2|J|$. With non-zero but modest interaction strength (Γ), transitions between MBL and ergodic phases can be similarly assessed based on the ratio $|V|/|J|$, with critical transition points numerically estimated in Ref. [59].

Before discussing variational optimization, we introduce a foundational observation based on our investigations in the preceding sections:

Observation 1 Consider an n -qubit Hamiltonian \hat{H} . For any k -local continuous subregion L and a factor $\xi \in [0, 1)$, there exists a finite kick strength $W \in [0, W^*)$ within the MBL phase such that for parameters θ Floquet-initialized in the set $\Theta_{\text{prd}}(W)$, the expected von Neumann entropy of the subsystem L in the output state $|\psi(\theta)\rangle$ satisfies:

$$\mathbb{E}_{\theta \in \Theta_{\text{prd}}(W)} S_L(|\psi(\theta)\rangle) < \xi S^{(Page)}(k, n). \quad (24)$$

This condition violates the weak barren plateaus criterion as defined in Ref. [20], implying that, on average, barren plateaus characterized by exponentially small variances do not occur.

To elucidate, weak barren plateaus are characterized by a scenario where the second Rényi entropy of a reduced density matrix for a region meets or exceeds a threshold dictated by the Page entropy, adjusted by a scaling factor within the range of $[0, 1)$. This definition suggests that when the entropy of a subsystem is proportionally high compared to the Page entropy, the optimization landscape is likely flat, exhibiting weak gradients across vast regions. However, our observation asserts that within the MBL phase, by selecting an adequately small kick strength W , it's possible to initialize a variational quantum circuit in a state that precludes the entropy of any subsystem from reaching levels that would indicate a weak barren plateau. Hence, this MBL initialization circumvents the exponential decay of gradients with increasing system size, mitigating the challenge posed by barren plateaus in quantum optimization in the early stage.

Barren Plateaus—We numerically substantiate observation 1 by comparing the initial gradients before optimization, $\nabla\langle\hat{\mathcal{H}}\rangle_\theta$, for the Floquet initialization with varying W . The trial state is drawn from an ensemble of products of single-qubit Haar-random states, and \hat{U}_t transforms the trial state into a computational basis state $|\varphi_c\rangle$, the energy associated with the initial parameters θ is computed as follows:

$$\langle\hat{\mathcal{H}}\rangle_\theta = \langle\varphi_c|\hat{U}(\theta)\hat{U}_t^\dagger\hat{\mathcal{H}}_{AA}\hat{U}_t\hat{U}(\theta)|\varphi_c\rangle. \quad (25)$$

For simplicity, we set the Hamiltonian parameters to the critical phase transition point without particle-particle interaction: α being the inverse golden ratio $(\sqrt{5}-1)/2$, $\phi = 0$, $J = 1$, $\Gamma = 0$, and $V = 2$. Fig. 3 illustrates the gradient infinity norm as a function of kick

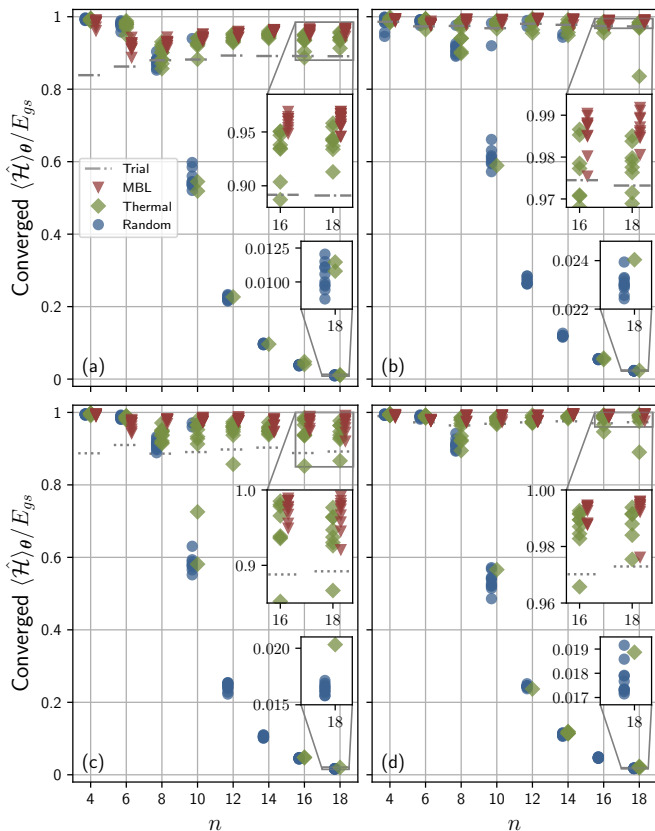


Figure 4. Converged approximation ratios from the variational quantum eigensolver for system sizes $n = 4, 6, 8, \dots, 18$ across 10 samples of initial parameters. This comparison illustrates the superiority of the MBL initialization ($W = 2/5$) over thermal ($W = 7/5$) and random strategies. (a) \hat{H}_{AA} in the extended phase ($\Gamma = 0, V = 1$). (b) \hat{H}_{AA} in the non-interacting Anderson localized phase ($\Gamma = 0, V = 4$). (c) \hat{H}_{AA} in the ergodic phase ($\Gamma = 1, V = 2$). (d) \hat{H}_{AA} in the MBL phase ($\Gamma = 3, V = 6$). Grey dotted lines mark the trial state energy, with insets providing a zoomed view for larger systems.

strength W for different system sizes, each point therein is averaged over 1000 samples. Within the MBL phase, the gradient remains protected and its norm decays exponentially with increasing W but does not vanish with growing system sizes. Conversely, in the thermal phase, the gradient norm exhibits exponential decay with n , indicating the presence of barren plateaus. Notably, although a scale-free point exists within the MBL phase, it does not serve as a definitive marker for the phase transition from MBL to thermal states.

Given the distinctive characteristic of the MBL phase, notably its preservation of initial information, we propose the following theorem to establish a bound on the gradient in the MBL phase under specific conditions:

Theorem 3 Consider a D -layer variational quantum circuit Floquet-initialized with parameters θ_{MBL} sampled from $\Theta_{\text{prd}}(W)$ where $W < W^*$. If the minimum absolute

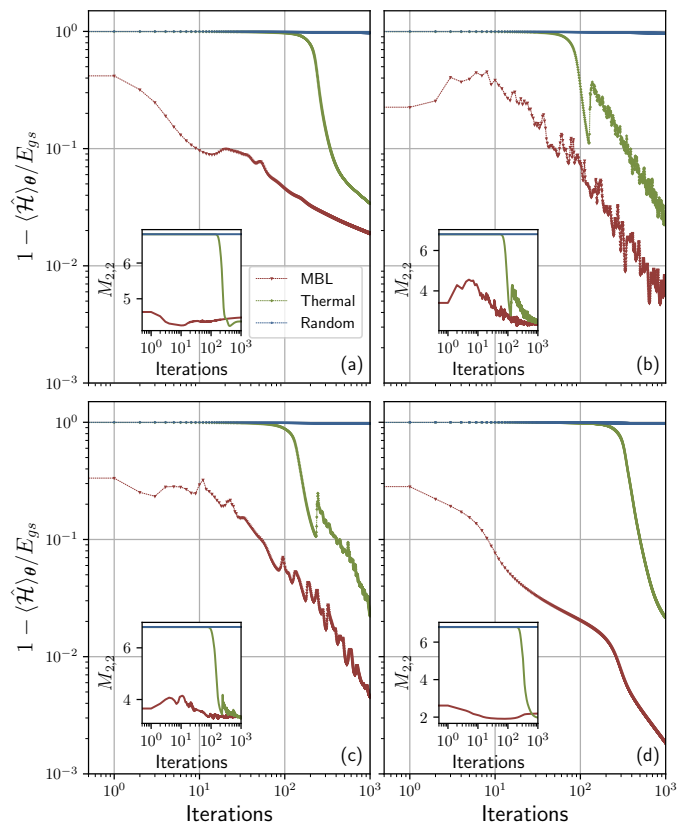


Figure 5. Relative energy error progression during optimization for a single set of initial parameters at $n = 14$. (a) \hat{H}_{AA} in the non-interacting Anderson localized phase ($\Gamma = 0, V = 4$). (b) \hat{H}_{AA} in the extended phase ($\Gamma = 0, V = 1$). (c) \hat{H}_{AA} in the MBL phase ($\Gamma = 3, V = 6$). (d) \hat{H}_{AA} in the ergodic phase ($\Gamma = 1, V = 2$). Insets show the low-weight stabilizer Rényi entropy $M_{2,2}$ throughout the optimization, emphasizing how initialization impacts energy convergence and entropy behaviors.

value of the output expectation value in the MBL phase, denoted as $\langle \hat{H} \rangle_{\text{MBL}}$, remains substantially non-zero, and a Floquet increase of N'_{kick} kick parameters (where N'_{kick} does not scale with system size and is of $\mathcal{O}(1)$) to W^* or $-W^*$ transitions the circuit out of the MBL phase, resulting in an average output expectation value of zero, then the expected infinity norm of the gradient of the Hamiltonian expectation value along this parameter path within the MBL phase is lower bounded by:

$$\mathbb{E}_{\theta_{\text{MBL}}} \left[\left\| \nabla \langle \hat{H} \rangle_{\theta} \right\|_{\infty} \right] \geq \frac{|\langle \hat{H} \rangle_{\text{MBL}}|}{D (2W^*)^{N'_{\text{kick}}}} \quad (26)$$

where $\tilde{\theta}_{\text{MBL}}$ denotes parameters along this transitional MBL path. The proof is given in Appendix E.

Optimization—We proceed with the optimization process by fixing the Hamiltonian parameters to $\alpha = (\sqrt{5} - 1)/2$, $\phi = 0$, and $J = 1$. We employ the variational

quantum eigensolver to prepare ground states of the one-dimensional \hat{H}_{AA} in different phases: non-interacting Anderson localized phase ($\Gamma = 0, V = 4$), extended phase ($\Gamma = 0, V = 1$), MBL phase ($\Gamma = 3, V = 6$), and ergodic phase ($\Gamma = 1, V = 2$). For the variational *Ansatz*, we use a 1D ring connectivity square circuit with a depth $D = n$. We investigate three distinct initialization strategies as follows:

- MBL initialization: Floquet initialization with steady parameters sampled from $[-\pi, \pi)$ and kick parameters sampled from $[-2/5, 2/5]$.
- Thermal initialization: Floquet initialization with steady parameters sampled from $[-\pi, \pi)$ and the kick parameters sampled from $[-7/5, 7/5]$.
- Random initialization: each parameter within each layer is uniformly sampled from $[-\pi, \pi)$.

We commence with a naive trial state $|\psi_t\rangle$ derived from an optimization of a low-dimensional matrix product state (MPS) featuring alternating bonds [60]. This MPS employs a bond dimension $\chi = 2$ between the $(2j - 1)$ -th and the $(2j)$ -th tensors, and $\chi = 1$ between the $(2j)$ -th and the $(2j + 1)$ -th tensors, for $j = 1, 2, \dots, n/2$. The quantum state corresponding to this MPS configuration is expressed as:

$$|\psi_t\rangle = \sum_{i_1, i_2, \dots, i_n} \left(\prod_{j=1}^{n/2} A^{i_{2j-1}, i_{2j}} \right) \left(\prod_{j=1}^{n/2-1} B^{i_{2j}, i_{2j+1}} \right) |i_1, i_2, \dots, i_n\rangle, \quad (27)$$

where $A^{i_{2j-1}, i_{2j}}$ are 2×2 tensor matrices for bonds of dimension $\chi = 2$ and $B^{i_{2j}, i_{2j+1}}$ are scalar values for bonds of dimension $\chi = 1$. These tensor parameters are finely tuned to minimize the trial energy $\langle \psi_t | \hat{H} | \psi_t \rangle$. The resulting state $|\psi_t\rangle$ is subsequently transformed to a computational basis state $|\varphi_c\rangle$ using a shallow quantum circuit \hat{U}_t , constituted by $(n/2)$ two-qubit gates:

$$|\varphi_c\rangle = \hat{U}_t |\psi_t\rangle = \prod_{j=1}^{n/2} \hat{U}_{2j-1, 2j} |\psi_t\rangle. \quad (28)$$

For our computations, $|\varphi_c\rangle$ is selected as the computational basis state exhibiting the highest overlap with $|\psi_t\rangle$.

We then proceed to the second stage – variational quantum optimization using a square circuit $\hat{U}(\boldsymbol{\theta})$. The initial parameters $\boldsymbol{\theta}$ are sampled, and we establish an appropriate learning rate (learning rate $\eta = 0.05$ for panels (a-c) and 0.01 for panel (d)). Optimization continues until the output energy converges within a specified tolerance of 0.001 or when the total number of iterations reaches 1000. The optimization employs a gradient descent algorithm, with parameter updates specified by:

$$\boldsymbol{\theta}' = \boldsymbol{\theta} - \eta \nabla \langle \hat{\mathcal{H}} \rangle_{\boldsymbol{\theta}}, \quad (29)$$

where $\boldsymbol{\theta}$ denotes the parameter values at the start of an iteration, and $\boldsymbol{\theta}'$ those after the iteration. Fig. 4 displays the converged relative energy error, defined as one minus the ratio of the converged energy to the ground state energy, for different system sizes and initialization strategies, with each point averaged over 10 samples of initial parameters. While the initial output states exhibit higher energy compared to the trial state for all initialization strategies, the MBL initialization consistently surpasses the trial state in subsequent optimizations, achieving an approximation ratio nearing unity across all phases of the target model \hat{H}_{AA} . In contrast, the performance of the random initialization strategy markedly deteriorates as system size increases, typically converging to a final state with an approximation ratio near 0 for system sizes up to 16 qubits. Meanwhile, although the thermal initialization shows a general decline as system size increases, it occasionally yields a low-energy state.

In addition to assessing initial gradients and final energy states, our study is fundamentally focused on the optimization trajectory. We aim to ascertain whether MBL-based initializations can steer the optimization process towards more advantageous paths that prevent convergence to a random output state. Fig. 5 presents numerical results for the relative energy error and the low-weight stabilizer Rényi entropy $M_{2,2}$ throughout the optimization process for all four phases with a single instance of the initial circuit parameters. This visualization indicates that thermal initialization outperforms random initialization, which struggles to overcome barren plateaus and achieve lower energy states even after 1,000 iterations. The MBL initialization demonstrates superior performance, with the energy of the output state rapidly approaching that of the ground state. Furthermore, the $M_{2,2}$ trajectory underscores that when the circuit is initialized in the MBL phase, the output state consistently deviates significantly from a random unitary 2-design state throughout the optimization process, crucially avoiding the risk of encountering barren plateaus, thereby enhancing the efficiency and potential success of the variational optimization.

V. EXPERIMENTAL VERIFICATION

In this section, we detail the experimental observation of the MBL to thermalization phase transition using Floquet-initialized variational quantum circuits on the *ibm_brisbane* quantum processor, a state-of-the-art superconducting quantum computing platform equipped with 127 qubits. Fig. 6(a) illustrates the architectural connectivity of the device, which includes 36 vertices connected to three qubits each, 89 vertices connected to two qubits, and 2 vertices connected to a single qubit. Table I lists the device's performance metrics, recorded during the experiments.

For clarity in our experimental setup, we focus on a specialized configuration of \hat{H}_{AA} with parameters $J = 1$,

Parameter	Median Value
# of qubits	127
T_1	232.17 μ s
T_2	153.64 μ s
ECR error	7.802×10^{-3}
SX error	2.428×10^{-4}
Readout error	1.370×10^{-2}
Error per layered gate	1.9%

Table I. Performance metrics of the *ibm.brisbane* quantum processor. Critical parameters include the number of qubits, coherence times (T_1 and T_2), error rates for echoed cross-resonance (ECR) gates and \sqrt{X} gates, readout error, and the average error per gate in a layered circuit configuration.

Setup	Qubits Used
$n = 13$	$Q_{73}, Q_{82-86}, Q_{92}, Q_{101-105}, Q_{111}$.
$n = 19$	$Q_{72}, Q_{78-84}, Q_{91}, Q_{92}, Q_{97-99}, Q_{101-105}, Q_{111}$.
$n = 25$	$Q_{72}, Q_{73}, Q_{78-88}, Q_{91-93}, Q_{97-99}, Q_{103-107}, Q_{111}$.
$n = 31$	$Q_{72}, Q_{73}, Q_{78-88}, Q_{91-93}, Q_{95-99}, Q_{103-107}, Q_{109}, Q_{111}, Q_{121-123}$.

Table II. Detailed qubits usage for different configurations with grouped subscript ranges

$V = \Gamma = -2J$, $\alpha = 0$, and $\phi = \pi$. This setup corresponds to the ferromagnetic Heisenberg model, governed by the Hamiltonian:

$$\hat{\mathcal{H}}_{\text{FH}} = -\frac{1}{2} \sum_{\substack{(j,k) \in \\ \text{edges}(G)}} (\hat{\sigma}_i^x \hat{\sigma}_j^x + \hat{\sigma}_i^y \hat{\sigma}_j^y + \hat{\sigma}_i^z \hat{\sigma}_j^z). \quad (30)$$

This model is implemented on an intermittently coupled spin chain of n qubits, where alternate qubits are linked to an additional, isolated qubit, leading to non-uniform interactions across all spins. This configuration aligns well with the connectivity graph of the *ibm.brisbane* quantum processor. Notably, the circuit layout is dynamically optimized by the Qiskit compiler for $W = 1/2$ to enhance performance in practical experiments. In one of our experiments, this configuration is applied to 31 qubits, depicted in Fig. 6(a) with red circles representing qubits and connecting edges.

Before the experiment, we numerically simulate the system using a Floquet initialization strategy where the rotation angles within $\hat{\mathcal{R}}_x$, $\hat{\mathcal{R}}_{xx}$, and $\hat{\mathcal{R}}_{yy}$ are uniformly sampled from the range $[-W, W]$. Our analysis focuses on the Pauli- XX rotation at the center of the first layer of the spin chain, which has been verified to accurately represent the global trend observed across the entire gradient profile. The associated rotation angle, θ_m , and its significant gradient magnitude indicate that the entire gradient landscape is likely safeguarded from barren plateaus

if one specific region shows avoidance. Considering our specific interest in observing phase transitions marked by the emergence and disappearance of significant gradients, we opt for a naive trial state in an alternating-spin Néel configuration, denoted as

$$|\psi_t\rangle = |\varphi_c\rangle = |\uparrow\rangle|\downarrow\rangle \cdots |\uparrow\rangle|\downarrow\rangle, \quad (31)$$

visually represented in Fig. 6(a). We measure the gradient of the Hamiltonian's expectation value relative to θ_m by executing each circuit configuration 4096 times. The circuit depth is set to $D = (n-1)/6$ for a system with n qubits, resulting in $5n(n-1)/6$ independent parameters. The average absolute gradient, depicted in Fig. 6(b) for 200 samples of initial parameters, displays a clear phase transition from MBL to thermalization around a critical point of $W_{\text{sim}}^* \approx 0.8$.

To initiate the experiment efficiently with limited resources, we employ a representative specialized sampling protocol for the initial Floquet circuit parameters, which includes all rotation angles within $\hat{\mathcal{R}}_x$, $\hat{\mathcal{R}}_z$, $\hat{\mathcal{R}}_{xx}$, $\hat{\mathcal{R}}_{yy}$, and $\hat{\mathcal{R}}_{zz}$. These parameters are generated using the zeros of the Chebyshev polynomial of the first kind, specifically:

$$\theta_j = \cos\left(\frac{(2j-1)\pi}{2(N_{\text{steady}}^{(1)} + N_{\text{kick}}^{(1)})}\right), \quad (32)$$

for $j = 1, 2, \dots, N_{\text{steady}}^{(1)} + N_{\text{kick}}^{(1)}$, where $N_{\text{steady}}^{(1)} = 2n$ and $N_{\text{kick}}^{(1)} = 3n$ represent the number of steady and kick parameters within the first layer, respectively. We arrange these zeros in a staggered pattern, placing positive zeros at even indices and negative zeros at odd indices within the rotation angle array. Subsequently, the rotation angles for $\hat{\mathcal{R}}_x$, $\hat{\mathcal{R}}_{xx}$, and $\hat{\mathcal{R}}_{yy}$ operations are scaled by the kick strength W to ensure they fall within the range $[-W, W]$. While readout error mitigation is applied to enhance measurement accuracy, gate error mitigation is intentionally omitted to preserve the intrinsic dynamics of the system.

The experiment is conducted across system sizes of $n = 13, 19, 25, 31$ using noisy physical qubits, as detailed in Table II. As shown in Fig. 6(c), the observed absolute gradient values display a gradual decline in magnitude as the kick parameter W is increased, signaling a transition towards the thermal phase. Despite the perturbing effects of noise, a discernible critical transition point is approximately identified at $W_{\text{exp}}^* \approx 1/2$. Below this threshold, gradient magnitudes are preserved to varying extents. Notably, this experimentally determined critical point is lower than the predicted value of $W_{\text{sim}}^* \approx 4/5$, highlighting the impact of hardware noise on shifting the observed critical threshold. However, the experimental results still corroborate the general theoretical trend.

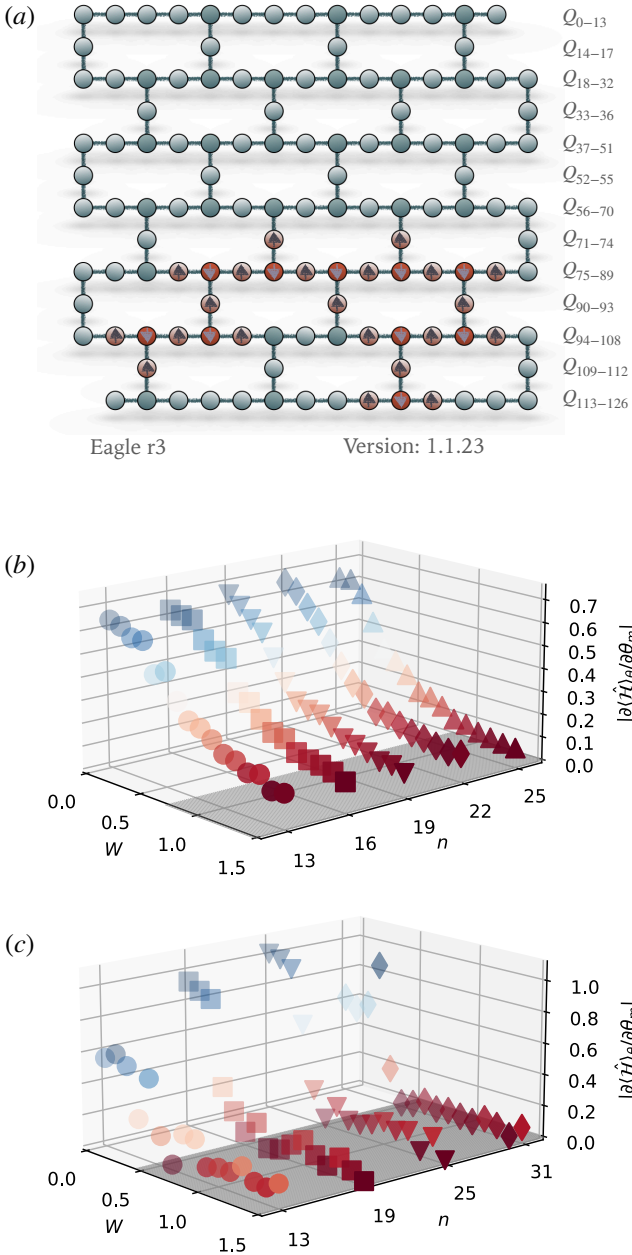


Figure 6. Experimental setup and analysis of the MBL-thermalization phase transition on IBM’s *ibm_brisbane* quantum processor. **(a)** Qubit layout of *ibm_brisbane* alongside an intermittently coupled spin chain, represented by red circles (qubits) and connecting edges (couplings). Arrows indicate the initial alternating-spin Néel configuration. **(b)** Simulation results of the observed gradients of the Hamiltonian’s expectation value as a function of the kick strength W for system sizes $n = 13, 16, 19, 21, 25$. **(c)** Experimental results for system sizes $n = 13, 19, 25, 31$, with gradients similarly demonstrating decay patterns as W increases, indicating a phase transition at an experimentally adjusted point $W^* \approx 1/2$. The experimental critical point is slightly shifted due to hardware noise.

VI. CONCLUSIONS AND OUTLOOK

The primary motivation behind this research was to address the significant challenge of barren plateaus in variational quantum simulation, a phenomenon that considerably impedes the scalability and efficiency of quantum optimization. This investigation explored the transition from many-body localization (MBL) to thermalization within a universal variational quantum circuit framework. We introduced an MBL-based strategy aimed at mitigating excessive entanglement and thereby circumventing barren plateaus in variational quantum optimization. The application of this protocol led to marked enhancements in energy convergence for the Aubry-André model across various phases, promoting more efficient optimization processes. A significant aspect of our study was the experimental validation of the phase transition on the 127-qubit *ibm_brisbane* quantum processor through gradient computation. Moreover, this research innovates by utilizing barren plateaus as a novel metric for identifying the critical point of the MBL-thermalization phase transition.

Our findings enhance the understanding of using MBL to overcome barren plateaus in variational quantum optimization, aligning with observations in Ref. [61] regarding the relationship between barren plateaus and classical simulability. This alignment is particularly evident in the early stages of optimization, given the classical simulability of MBL systems [62]. Despite this, our methodology is designed to maintain substantial optimization gradients, even potentially during a transition to a thermal phase, suggesting a pathway to transcend classical simulability. Thus, our protocol strikes a balance between avoiding gradient vanishing and sustaining a quantum advantage.

This work opens several promising avenues for future research. One potential direction involves applying the MBL-based initialization protocol to quantum machine learning tasks, such as quantum generative adversarial networks [63]. Utilizing the unique properties of MBL systems could potentially lead to more efficient and trainable quantum machine learning algorithms capable of generating distributions beyond the capabilities of classical methods. Further, exploring the interplay between MBL and other aspects of quantum circuits, such as measurement-induced phase transitions [21] and information scrambling [64], could yield valuable insights into quantum dynamics. Additionally, employing MBL in specialized variational quantum protocols, including the quantum approximate optimization algorithm [11, 12, 65, 66] and the variational simulation of time evolution [67, 68], presents further exploration possibilities.

However, several open questions and potential enhancements persist within our framework. One critical issue is the selection of optimal trial states whose entanglement structures align closely with those of the target system’s ground state. This alignment is crucial for enhancing the efficiency of quantum optimization but re-

mains a complex challenge. If trial states are generated from matrix product states with higher bond dimensions, methodologies outlined in Refs. [69–71] could be utilized to decompose these states into computational basis states using log-depth shallow circuits, potentially simplifying this process. Another significant consideration is the quantitative assessment of hardware noise effects on the critical points of MBL and thermalization phases. Fully understanding how this factor influences the transition points and the overall dynamics of variational quantum circuits is essential for enhancing their practical effectiveness. Additionally, integrating MBL initialization with advanced techniques such as joint Bell measurements or circuit parallelism could significantly accelerate optimization processes [72, 73].

Note added. After the completion of this manuscript, we became aware of Ref. [74], a related preprint that discusses an alternative MBL initialization protocol with different setups from our study.

ACKNOWLEDGMENTS

We thank Paul Skrzypczyk, Luya Lou, Yunlong Yu, Tianyi Hao, Qihao Guo, Zheng-Hang Sun, B. Özgüler, and M. Vavilov for helpful discussions. This work was supported by the Theory of Quantum Matter Unit, OIST. We acknowledge the use of IBM Quantum services for this work.

Appendix A: Universality of the variational *Ansatz*

Observation 2 *The variational quantum circuits depicted in Fig. 1 is capable of approximating any arbitrary quantum operation or unitary transformation to an arbitrary level of accuracy, given a sufficient number of qubits and circuit layers.*

Proof Consider any pair of adjacent qubits, denoted as Q_j and Q_k . We can construct a layout with 15 parameterized gates in three consecutive layers, as depicted in Fig. 7. It is known that any single-qubit unitary operation can be achieved through consecutive rotations of Pauli- $Z - X - Z$ or Pauli- $X - Z - X$, up to a global phase. Moreover, the operation

$$\exp\left(-i\frac{\theta_{xx}}{2}\hat{\sigma}_j^x\hat{\sigma}_k^x\right)\exp\left(-i\frac{\theta_{yy}}{2}\hat{\sigma}_j^y\hat{\sigma}_k^y\right)\exp\left(-i\frac{\theta_{zz}}{2}\hat{\sigma}_j^z\hat{\sigma}_k^z\right) \quad (\text{A1})$$

is equivalent to the operation

$$\exp\left(-i\frac{\theta_{xx}}{2}\hat{\sigma}_j^x\hat{\sigma}_k^x - i\frac{\theta_{yy}}{2}\hat{\sigma}_j^y\hat{\sigma}_k^y - i\frac{\theta_{zz}}{2}\hat{\sigma}_j^z\hat{\sigma}_k^z\right). \quad (\text{A2})$$

Consequently, we can employ Cartan’s KAK decomposition [75]:

$$\begin{aligned} \hat{U}(\boldsymbol{\theta}) &= \hat{U}_s(\theta_1, \theta_2, \theta_3) \otimes \hat{U}_s(\theta_4, \theta_5, \theta_6) \\ &\exp\left(-i\frac{\theta_7}{2}\hat{\sigma}_j^x\hat{\sigma}_k^x - i\frac{\theta_8}{2}\hat{\sigma}_j^y\hat{\sigma}_k^y - i\frac{\theta_9}{2}\hat{\sigma}_j^z\hat{\sigma}_k^z\right) \quad (\text{A3}) \\ &\hat{U}_s(\theta_{10}, \theta_{11}, \theta_{12}) \otimes \hat{U}_s(\theta_{13}, \theta_{14}, \theta_{15}), \end{aligned}$$

where $\hat{U}_s(\theta_\alpha, \theta_\beta, \theta_\gamma)$ represents a 3-parameter universal single-qubit unitary acting on Q_j or Q_k . Any two-qubit unitary operation $\hat{U} \in SU(4)$ can be decomposed into the KAK form. As a result, we can implement arbitrary 1-qubit and 2-qubit gates, such as the universal gate set {CNOT, H, S, T}. In addition, we can perform swap gates between adjacent qubits, enabling us to apply a universal gate set on any two qubits. Thus the Solovay–Kitaev theorem [76] applies and we can approximate any unitary transformation to an arbitrary level of accuracy, provided that there are a sufficient number of qubits and circuit layers. ■

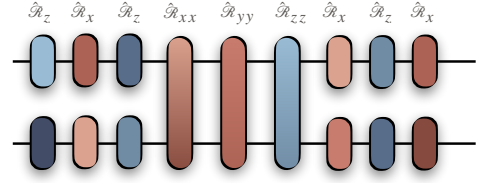


Figure 7. Cartan’s KAK decomposition of arbitrary double-qubit unitary $U \in SU(4)$.

Appendix B: Proof of Theorem 1

Proof When $\{\hat{U}(\boldsymbol{\theta})\}$ with $\boldsymbol{\theta}$ uniformly sampled from Θ forms a unitary t -design, the output state ensemble $\{|\psi(\boldsymbol{\theta})\rangle = \hat{U}(\boldsymbol{\theta})|\psi_{\text{in}}\rangle\}$ for arbitrary input state $|\psi_{\text{in}}\rangle$ mimics Haar random states with respect to the t -th order moments. Therefore we have

$$\begin{aligned} \int_{\Theta} \text{IPR}_t(|\psi(\boldsymbol{\theta})\rangle) d\boldsymbol{\theta} &= \int_{\Theta} \sum_j |\langle \beta_j | \psi(\boldsymbol{\theta}) \rangle|^{2t} d\boldsymbol{\theta} \\ &= \int_{\Theta} \sum_j |\langle \beta_j |^{\otimes t} \psi(\boldsymbol{\theta})^{\otimes t} |^{2t} d\boldsymbol{\theta} \quad (\text{B1}) \\ &= \frac{2^n}{d_{\text{sym}}^{(t)}} \end{aligned}$$

The dimension of the t -fold symmetric subspace

$$d_{\text{sym}}^{(t)} = \binom{t + 2^n - 1}{t}, \quad (\text{B2})$$

therefore

$$\int_{\Theta} \text{IPR}_t(|\psi(\boldsymbol{\theta})\rangle) d\boldsymbol{\theta} = \frac{2^n t!}{(t + 2^n - 1)!}. \quad (\text{B3})$$

When $t = 2$, the ensemble $\{|\psi(\boldsymbol{\theta})\rangle = \hat{U}(\boldsymbol{\theta})|\psi_{\text{in}}\rangle\}$ mimics Haar random states for quadratic functions, we have

$$\int_{\Theta} \text{IPR}_2(|\psi(\boldsymbol{\theta})\rangle) d\boldsymbol{\theta} = \frac{2}{(2^n + 1)}. \quad (\text{B4})$$

■

Appendix C: State 2-Design and Circuit Expressibility

As previously noted in Section III, although the inverse participation ratio (IPR_t) can suggest whether a quantum state ensemble deviates from forming a unitary t -design, it is not solely sufficient for such a determination. To provide further evidence that the ensembles transition into unitary 2-designs within the thermal phase, we investigate the frame potential, defined for t -th order moments as:

$$\mathcal{F}_t = \int_{\Theta} \int_{\Theta} |\langle \psi(\boldsymbol{\theta}_1) | \psi(\boldsymbol{\theta}_2) \rangle|^{2t} d\boldsymbol{\theta}_1 d\boldsymbol{\theta}_2. \quad (\text{C1})$$

An ensemble qualifies as a unitary t -design if its frame potential matches the Haar measure frame potential, known as the Welch bounds:

$$\mathcal{F}_t = \mathcal{F}_t^{(\text{Haar})} := \frac{1}{d^{(t)}_{\text{sym}}} = \frac{1}{\binom{t+2^n-1}{t}}. \quad (\text{C2})$$

For a unitary 2-design in particular, this criterion simplifies to:

$$\mathcal{F}_2 = \mathcal{F}_2^{(\text{Haar})} := \frac{2}{2^n(2^n + 1)}. \quad (\text{C3})$$

We calculate the average frame potentials \mathcal{F}_2 , \mathcal{F}_4 , and \mathcal{F}_6 across various values of W , and present these findings in Fig. 8 (a-f). In the thermal phase, these averaged frame potentials accurately reflect their theoretical Haar values, substantiating the ensemble's transition to unitary designs.

Additionally, the ratio between \mathcal{F}_2 and $\mathcal{F}_2^{(\text{Haar})}$ is indicative of the circuit's state-dependent expressibility [22], defined as:

$$\varepsilon_t(|\psi_t\rangle\langle\psi_t|) := \left\| \int_{\Theta} \left(\hat{U}(\boldsymbol{\theta}) \right)^{\otimes t} (|\psi_t\rangle\langle\psi_t|^{\otimes t}) \left(\hat{U}^\dagger(\boldsymbol{\theta}) \right)^{\otimes t} d\boldsymbol{\theta} - \int_{\mathcal{U}} \hat{U}^{\otimes t} (|\psi_t\rangle\langle\psi_t|^{\otimes t}) \left(\hat{U}^\dagger \right)^{\otimes t} d\mu_H(\hat{U}) \right\|_2. \quad (\text{C4})$$

Here, our trial state $|\psi_t\rangle$ is sampled from the computational basis. Larger ratios suggest reduced expressibility of the *Ansatz*, whereas ratios approaching 1 indicate maximal expressibility associated with strong barren plateaus. Fig. 8 (g) shows these ratios for the MBL phase ($W = \pi/10$) and the thermal phase ($W = 9\pi/20$) in the 1D ring topology, and Fig. 8 (h) for the MBL phase ($W = \pi/20$) and the thermal phase ($W = 9\pi/40$) in the

$\text{Ci}_n(1, 2)$ lattice topology. In the MBL phase, these ratios exponentially increase with the system size n , indicating limited expressibility, whereas in the thermal phase, they remain constant near 1, indicative of maximal expressibility.

Appendix D: Proof of Theorem 2

For traceless operator \hat{O} , consider its eigenstates corresponding to eigenvalues $\pm\lambda$ as $|p_j\rangle_{j=1,2,\dots,N/2}$ and $|m_j\rangle_{j=1,2,\dots,N/2}$, respectively. The t -fold product of $\hat{O}^{\otimes t}$ can be decomposed to orthogonal Hermitian terms with permutation symmetry under the permutation group \mathcal{S}_t . We denote the positive and negative eigenvalue terms as \mathcal{Q}^+ and \mathcal{Q}^- , respectively, then denote $\mathcal{Q} = \mathcal{Q}^+ \cup \mathcal{Q}^-$. The cardinality of the set of these terms equals the dimension of the completely symmetric subspace, \mathcal{S}_t , given by:

$$\text{card}(\mathcal{Q}) = d_{\text{sym}}^{(t)} = \binom{N+t-1}{t}. \quad (\text{D1})$$

As an example, we show one term in \mathcal{Q}^+ :

$$\hat{Q}_1^+ = \lambda^t |p_1\rangle\langle p_1| \otimes |p_1\rangle\langle p_1| \otimes \cdots \otimes |p_1\rangle\langle p_1|, \quad (\text{D2})$$

and one term in \mathcal{Q}^- :

$$\begin{aligned} \hat{Q}_1^- &= -\lambda^t |m_1\rangle\langle m_1| \otimes |p_1\rangle\langle p_1| \otimes \cdots \otimes |p_1\rangle\langle p_1| \\ &\quad - \lambda^t |p_1\rangle\langle p_1| \otimes |m_1\rangle\langle m_1| \otimes \cdots \otimes |p_1\rangle\langle p_1| \\ &\quad \dots \\ &\quad - \lambda^t |p_1\rangle\langle p_1| \otimes |p_1\rangle\langle p_1| \otimes \cdots \otimes |m_1\rangle\langle m_1|. \end{aligned} \quad (\text{D3})$$

Consider $\{|\psi\rangle\}$, an ensemble of n -qubit quantum states that forms state t -design. Using the t -design properties, we have

$$\mathbb{E}_{|\psi\rangle} \text{Tr} \left(\hat{Q}_j^+ |\psi\rangle^{\otimes t} \langle\psi|^{\otimes t} \right) = \lambda^t / \binom{N+t-1}{t} \quad (\text{D4})$$

for $\hat{Q}_j^+ \in \mathcal{Q}^+$, and

$$\mathbb{E}_{|\psi\rangle} \text{Tr} \left(\hat{Q}_j^- |\psi\rangle^{\otimes t} \langle\psi|^{\otimes t} \right) = -\lambda^t / \binom{N+t-1}{t} \quad (\text{D5})$$

for $\hat{Q}_j^- \in \mathcal{Q}^-$.

To estimate the expected value $\mathbb{E}_{|\psi\rangle} \langle\psi|\hat{O}|\psi\rangle^t$, it is essential to determine the difference in cardinalities between the sets \mathcal{Q}^+ and \mathcal{Q}^- . Initially disregarding the eigenvalues $+\lambda$ or λ , we focus solely on the combinations of lower indices $\alpha \in \{1, 2, \dots, N/2\}$. For any operator \hat{Q}_j^- in \mathcal{Q}^- , there is at least one index α such that each term of \hat{Q}_j^- has an odd number of tensors with indices α . For these combinations of indices, the number of terms in \mathcal{Q}^+ equals the number of terms in \mathcal{Q}^- . Next, we consider index combinations where each index appears an

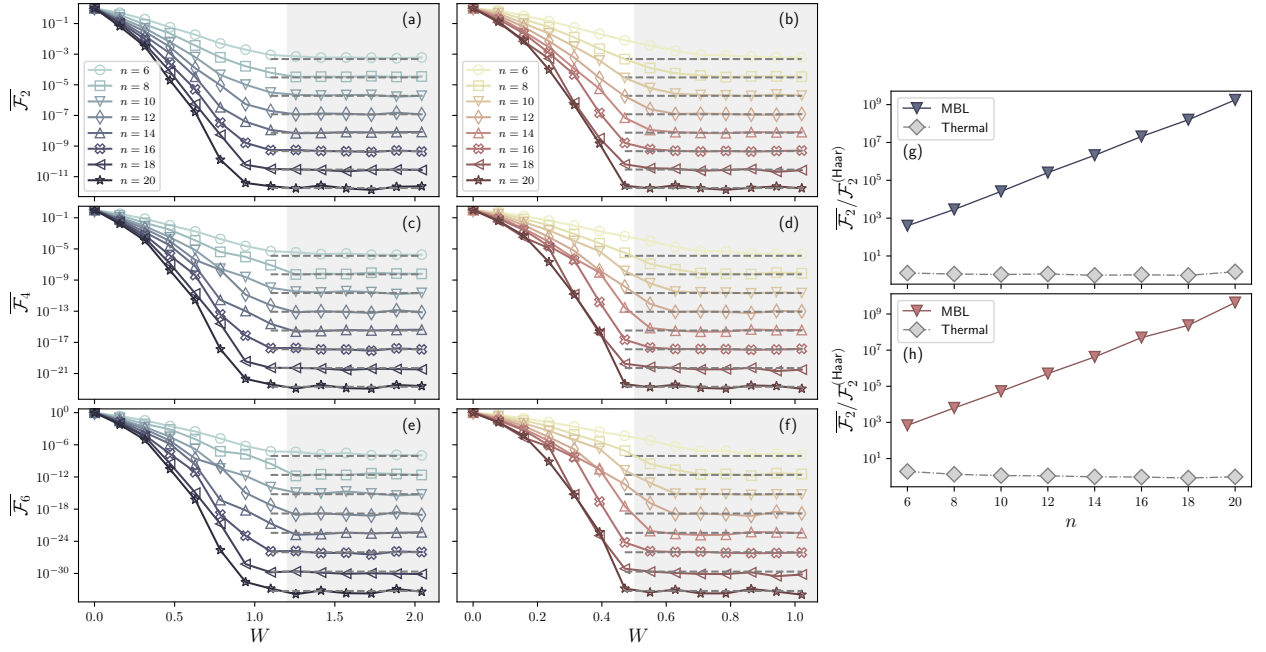


Figure 8. Frame potentials of output states across different orders as a function of kick strength W for various lattice topologies, demonstrating how close the ensembles approach unitary t -designs. (a, c, e) display results for the 1D ring topology. (b, d, f) show results for the $\text{Ci}_n(1, 2)$ lattice topology. Each panel presents frame potentials of different orders: (a, b) second-order, (c, d) fourth-order, and (e, f) sixth-order. Data averaged over 100 samples, with grey dashed lines indicating the Welch bounds [77]. (g) and (h) illustrate the ratios between the computed frame potentials and the corresponding Haar random frame potentials for the 1D ring and the $\text{Ci}_n(1, 2)$ lattice, respectively.

even number of times. The total number of such index combinations is $\binom{N/2+t/2-1}{t/2}$. For these combinations, the number of terms in \mathcal{Q}^+ exceeds those in \mathcal{Q}^- by one. Consequently, we conclude that:

$$\text{card}(\mathcal{Q}^+) - \text{card}(\mathcal{Q}^-) = \binom{N/2+t/2-1}{t/2}. \quad (\text{D6})$$

Therefore, the expected value of $\mathbb{E}_{|\psi\rangle} \langle \psi | \hat{O} | \psi \rangle^t$ over the ensemble is computed as follows:

$$\begin{aligned} \mathbb{E}_{|\psi\rangle} \langle \psi | \hat{O} | \psi \rangle^t &= \mathbb{E}_{|\psi\rangle} \text{Tr} \left(\hat{O}^{\otimes t} |\psi\rangle^{\otimes t} \langle \psi|^{\otimes t} \right) \\ &= \sum_{\hat{Q}_j \in \mathcal{Q}} \mathbb{E}_{|\psi\rangle} \text{Tr} \left(\hat{Q}_j |\psi\rangle^{\otimes t} \langle \psi|^{\otimes t} \right) \\ &= \frac{\lambda^t \binom{N/2+t/2-1}{t/2}}{\binom{N+t-1}{t}}. \end{aligned} \quad (\text{D7})$$

When $\{\hat{U}(\theta)\}$ with θ uniformly sampled from Θ forms a unitary t -design, the ensemble of the output states for any arbitrary n -qubit input state forms a state t -design, yielding:

$$\int_{\Theta} \langle \psi(\theta) | \hat{O} | \psi(\theta) \rangle^t d\theta = \frac{\lambda^t \binom{N/2+t/2-1}{t/2}}{\binom{N+t-1}{t}}. \quad (\text{D8})$$

The low-weight Pauli set, denoted as $\mathcal{P}_{n,k}$, includes one identity operator and $\text{card}(\mathcal{P}_{n,k}) - 1$ non-identity Pauli

tensor product. Each non-identity tensor product in this set is a traceless observable \hat{O} with eigenvalues $+1$ and -1 . Therefore, the integral over the ensemble for these Pauli operators, weighted by their cardinality, is given by:

$$\begin{aligned} &\int_{\Theta} \sum_{\hat{P} \in \mathcal{P}_{n,k}} \frac{\langle \psi(\theta) | \hat{P} | \psi(\theta) \rangle^{2t}}{\text{card}(\mathcal{P}_{n,k})} d\theta \\ &= \frac{1}{\text{card}(\mathcal{P}_{n,k})} + (\text{card}(\mathcal{P}_{n,k}) - 1) \frac{\binom{2^{n-1}+t/2-1}{t/2}}{\binom{2^n+t-1}{t}} \\ &= \frac{\binom{2^n+t-1}{t} - \binom{2^{n-1}+t/2-1}{t/2}}{\text{card}(\mathcal{P}_{n,k}) \binom{2^n+t-1}{t}} + \frac{\binom{2^{n-1}+t/2-1}{t/2}}{\binom{2^n+t-1}{t}}. \end{aligned} \quad (\text{D9})$$

This equation articulates the relationship between the frame potentials of states generated under the influence of low-weight Pauli operators and their respective probabilities within the ensemble, as established by Theorem 2.

Appendix E: Proof of Theorem 3

In our variational quantum circuit, parameterized by N_{steady} steady parameters and N_{kick} kick parameters, we specifically focus on N'_{kick} kick parameters, where N'_{kick} is of order $\mathcal{O}(1)$ and does not scale with the system size. These parameters are the same across D layers due to the

Floquet initialization, and are collectively represented as:

$$\boldsymbol{\theta}_{\text{MBL}} = (\theta_1^{(1)}, \theta_2^{(1)}, \dots, \theta_{N'_{\text{kick}}}^{(1)}, \theta_1^{(2)}, \theta_2^{(2)}, \dots, \theta_{N'_{\text{kick}}}^{(D)}), \quad (\text{E1})$$

where $\theta_j^{(1)} = \theta_j^{(2)} = \dots = \theta_j^{(D)}$ for each j .

Consider the transition of these parameters from their initial values in the MBL phase ($\boldsymbol{\theta}_{\text{MBL}}$) to values in the thermal phase ($\boldsymbol{\theta}_{\text{thermal}}$). The maximum differential is bounded by $2W^*$, assuming the parameter transition could go from $-W^*$ to W^* .

The total change in $\langle \hat{H} \rangle_{\boldsymbol{\theta}}$ from $\boldsymbol{\theta}_{\text{MBL}}$ to $\boldsymbol{\theta}_{\text{thermal}}$ can be expressed as:

$$\Delta \langle \hat{H} \rangle = \int_{\boldsymbol{\theta}_{\text{MBL}}}^{\boldsymbol{\theta}_{\text{thermal}}} \nabla \langle \hat{H} \rangle \cdot d\boldsymbol{\theta} \quad (\text{E2})$$

where:

$$\Delta \langle \hat{H} \rangle = \langle \hat{H} \rangle_{\text{thermal}} - \langle \hat{H} \rangle_{\text{MBL}} = -\langle \hat{H} \rangle_{\text{MBL}}. \quad (\text{E3})$$

Decomposing the change into contributions from each parameter, assuming they vary concurrently within all layers, we have:

$$|\Delta \langle \hat{H} \rangle| = \left| \int_{\theta_{\text{MBL},1}}^{\theta_{\text{thermal},1}} \dots \int_{\theta_{\text{MBL},N'_{\text{kick}}}}^{\theta_{\text{thermal},N'_{\text{kick}}}} \nabla' \langle \hat{H} \rangle \cdot d\boldsymbol{\theta} \right| \quad (\text{E4})$$

$$\leq \overline{\|\nabla' \langle \hat{H} \rangle\|_{\infty}} \left(\sum_{j=1}^{N'_{\text{kick}}} |\theta_{\text{thermal},j} - \theta_{\text{MBL},j}| \right) \quad (\text{E5})$$

$$\leq \overline{\|\nabla' \langle \hat{H} \rangle\|_{\infty}} (2W^*)^{N'_{\text{kick}}} \quad (\text{E6})$$

Here, ∇' denotes the gradient under the Floquet constraint, and the overline denotes averaging over the parameter transition path. Now we abandon the constraint and consider independent parameters across layers, we can refine the inequality to:

$$|\Delta \langle \hat{H} \rangle| \leq \mathbb{E}_{\tilde{\boldsymbol{\theta}}_{\text{MBL}}} \left[\|\nabla \langle \hat{H} \rangle\|_{\infty} \right] D (2W^*)^{N'_{\text{kick}}} \quad (\text{E7})$$

Thus, the expected infinity norm of the gradient of the Hamiltonian expectation value along this parameter path within the MBL phase is lower bounded by:

$$\mathbb{E}_{\tilde{\boldsymbol{\theta}}_{\text{MBL}}} \left[\|\nabla \langle \hat{H} \rangle_{\boldsymbol{\theta}}\|_{\infty} \right] \geq \frac{|\langle \hat{H} \rangle_{\text{MBL}}|}{D (2W^*)^{N'_{\text{kick}}}} \quad (\text{E8})$$

This proof confirms the robust gradient presence in the MBL phase.

Appendix F: Dynamics of Deep Circuits

In this section, we employ our Floquet initialization strategy while substantially extending the circuit depth to investigate the dynamics of deep quantum circuits. We examine the output expectation values of Pauli $\hat{\sigma}_j^z$ on the first qubit over a range of circuit depths D . We

utilize both many-body localization (MBL) and thermal initializations to explore their distinct dynamics. Specifically, we apply a kick strength of $W = 0.2$ for the 1D ring topology and $W = 0.1$ for the $\text{Ci}_n(1,2)$ lattice topology under MBL conditions, and set the strengths to $W = 1.4$ for the 1D ring and $W = 0.7$ for the $\text{Ci}_n(1,2)$ under thermal conditions. The results are illustrated in Fig. 9(a-d). Remarkably, the local information in the MBL phase remains robustly preserved even beyond 1000 layers, underscoring the effectiveness of MBL dynamics in protecting initial system information within extremely deep circuits. This preservation sharply contrasts with the outcomes from circuits without Floquet initialization, where local information typically diminishes as circuit depth increases. We provide a comparative analysis by showing results from circuits with non-Floquet initialization, where each parameter is independently sampled from a narrow range of $[-0.2, 0.2]$ for the 1D ring and $[-0.1, 0.1]$ for the $\text{Ci}_n(1,2)$ lattice. The results, depicted in Fig. 9(e,f), demonstrate that the initial local information is entirely lost after approximately 100 iterations. Despite significant fluctuations observed over extended periods, the MBL phase distinctly demonstrates its capacity to mitigate the loss of local information, reflecting the characteristic resilience of standard many-body localized systems.

Without loss of generality, we focus on the fluctuations of the output expectation values for circuit depths D ranging from 500 to 1500, using $N = 1000$ data points in a 16-qubit system. Initially, we apply linear regression to detrend the original data:

$$y_D = \langle \hat{\sigma}_1^z \rangle_D - \overline{\langle \hat{\sigma}_1^z \rangle} - f(D), \quad (\text{F1})$$

where $f(D)$ represents the linear regression function fitted to the data. To mitigate spectral leakage in the power spectral density (PSD) analysis [78], we employ a window function:

$$\tilde{y}_D = y_D \cdot w_D, \quad (\text{F2})$$

where w_D is the Hanning window, defined as:

$$w_D = \frac{1}{2} \left(1 - \cos \left(\frac{2\pi D}{N-1} \right) \right). \quad (\text{F3})$$

Subsequently, we calculate the discrete Fourier transform of the windowed data using the fast Fourier transform algorithm:

$$Y_k = \sum_{D=0}^{N-1} \tilde{y}_D \cdot e^{-i\frac{2\pi k D}{N}}, \quad (\text{F4})$$

where Y_k represents the k -th element of the Fourier transform. The PSD, P_k , is determined by taking the square of the absolute value of Y_k and normalizing by the number of data points:

$$\text{PSD}_k = \frac{|Y_k|^2}{N}. \quad (\text{F5})$$

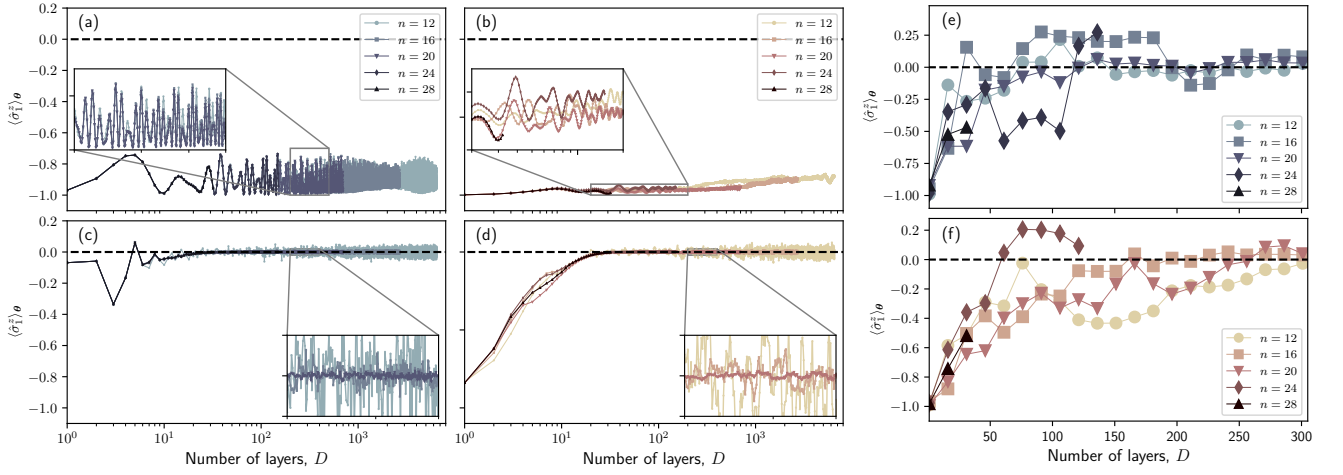


Figure 9. Demonstration of many-body localization within a circuit model, showcasing the output expectation values from deep variational quantum circuits across different phases and initializations. **(a, c)** Illustrate results for a 1D ring topology under MBL conditions with kick strengths $W = 1/5$ and $W = 7/5$ respectively, highlighting the preservation of local information even at greater circuit depths. **(b, d)** Display outcomes for a $C_{i_n}(1,2)$ lattice topology with kick strengths $W = 1/10$ and $W = 7/10$ respectively, reflecting the dynamics across both MBL and thermal phases. **(e, f)** Compare these with results from non-Floquet-initialized circuits for the same topologies but with each parameter independently sampled from narrow ranges $[-1/5, 1/5]$ and $[-1/10, 1/10]$, respectively. These panels demonstrate a rapid loss of local information within about 100 layers, starkly contrasting with the robustness observed in the Floquet-initialized systems depicted in panels (a-d).

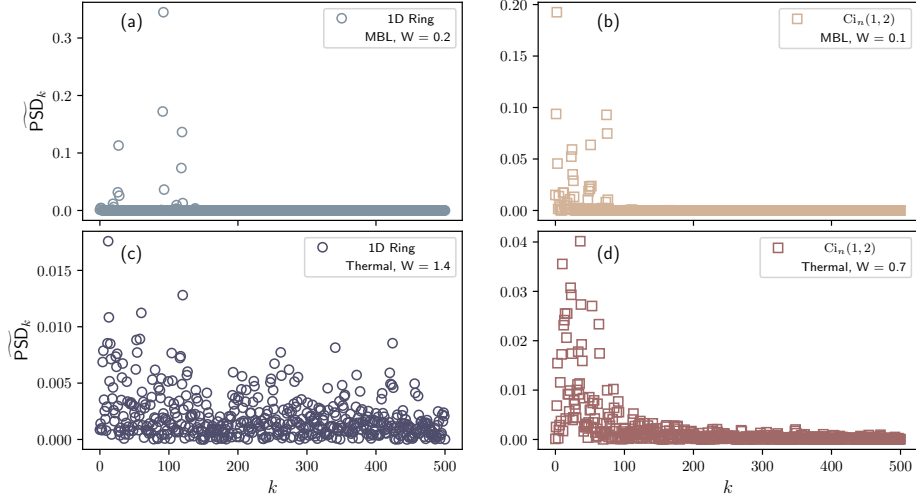


Figure 10. Power spectrum analysis of the output state expectation value fluctuations for $\hat{\sigma}_1^z$ in a 16-qubit system, with circuit depth D varying from 100 to 500. This analysis continues using our Floquet initialization strategy, extending the circuit depth significantly. Panels **(a, c)** illustrate results for a 1D ring topology with kick strengths $W = 0.2, 1.4$, respectively; panels **(b, d)** display the $C_{i_n}(1,2)$ lattice topology with kick strengths $W = 0.1, 0.7$, respectively.

The PSD is then normalized by dividing each element by the total power, which is the sum of all PSD values:

$$\widetilde{PSD}_k = \frac{PSD_k}{\sum_{j=0}^{N/2} PSD_j}. \quad (\text{F6})$$

The resulting normalized spectrum, \widetilde{PSD}_k , illustrated in Fig. 10, reveals distinct characteristics of the circuit dynamics across different phases. In the MBL phase, the power spectrum displays several prominent peaks, indica-

tive of multiple dominant frequency components. This suggests that the circuit's dynamical evolution is characterized by various periodic patterns with distinct frequencies. Conversely, in the thermal phase, the power spectrum exhibits a more uniform distribution of frequencies with fewer dominant components. This notable difference in spectral characteristics between the MBL and thermal phases provides a compelling diagnostic tool for characterizing and distinguishing the dynamical behavior of variational quantum circuits in different operational phases.

- [1] J. Preskill, *Quantum* **2**, 79 (2018).
- [2] M. Cerezo, A. Arrasmith, R. Babbush, S. C. Benjamin, S. Endo, K. Fujii, J. R. McClean, K. Mitarai, X. Yuan, L. Cincio, and P. J. Coles, *Nature Reviews Physics* **3**, 625 (2021).
- [3] K. Bharti, A. Cervera-Lierta, T. H. Kyaw, T. Haug, S. Alperin-Lea, A. Anand, M. Degroote, H. Heimonen, J. S. Kottmann, T. Menke, W.-K. Mok, S. Sim, L.-C. Kwek, and A. Aspuru-Guzik, *Rev. Mod. Phys.* **94**, 015004 (2022).
- [4] J. R. McClean, S. Boixo, V. N. Smelyanskiy, R. Babbush, and H. Neven, *Nature Communications* **9**, 4812 (2018).
- [5] C. Ortiz Marrero, M. Kieferová, and N. Wiebe, *PRX Quantum* **2**, 040316 (2021).
- [6] M. Larocca, P. Czarnik, K. Sharma, G. Muraleedharan, P. J. Coles, and M. Cerezo, *Quantum* **6**, 824 (2022).
- [7] E. Cervero Martín, K. Plekhanov, and M. Lubasch, *Quantum* **7**, 974 (2023).
- [8] M. Larocca, S. Thanasilp, S. Wang, K. Sharma, J. Biamente, P. J. Coles, L. Cincio, J. R. McClean, Z. Holmes, and M. Cerezo, A review of barren plateaus in variational quantum computing (2024), [arXiv:2405.00781](https://arxiv.org/abs/2405.00781) [quant-ph].
- [9] A. Peruzzo, J. McClean, P. Shadbolt, M.-H. Yung, X.-Q. Zhou, P. J. Love, A. Aspuru-Guzik, and J. L. O'Brien, *Nature Communications* **5**, 4213 (2014).
- [10] D. Wecker, M. B. Hastings, and M. Troyer, *Phys. Rev. A* **92**, 042303 (2015).
- [11] E. Farhi, J. Goldstone, and S. Gutmann, A quantum approximate optimization algorithm (2014), [arXiv:1411.4028](https://arxiv.org/abs/1411.4028) [quant-ph].
- [12] L. Zhou, S.-T. Wang, S. Choi, H. Pichler, and M. D. Lukin, *Phys. Rev. X* **10**, 021067 (2020).
- [13] D. Gross, S. T. Flammia, and J. Eisert, *Phys. Rev. Lett.* **102**, 190501 (2009).
- [14] M. Cerezo, A. Sone, T. Volkoff, L. Cincio, and P. J. Coles, *Nature Communications* **12**, 1791 (2021).
- [15] H.-K. Zhang, S. Liu, and S.-X. Zhang, *Phys. Rev. Lett.* **132**, 150603 (2024).
- [16] A. A. Mele, G. B. Mbeng, G. E. Santoro, M. Collura, and P. Torta, *Phys. Rev. A* **106**, L060401 (2022).
- [17] R. Wiersema, C. Zhou, Y. de Sereville, J. F. Carrasquilla, Y. B. Kim, and H. Yuen, *PRX Quantum* **1**, 020319 (2020).
- [18] C.-Y. Park and N. Killoran, *Quantum* **8**, 1239 (2024).
- [19] T. L. Patti, K. Najafi, X. Gao, and S. F. Yelin, *Phys. Rev. Res.* **3**, 033090 (2021).
- [20] S. H. Sack, R. A. Medina, A. A. Michailidis, R. Kueng, and M. Serbyn, *PRX Quantum* **3**, 020365 (2022).
- [21] R. Wiersema, C. Zhou, J. F. Carrasquilla, and Y. B. Kim, *SciPost Phys.* **14**, 147 (2023).
- [22] Z. Holmes, K. Sharma, M. Cerezo, and P. J. Coles, *PRX Quantum* **3**, 010313 (2022).
- [23] P. W. Anderson, *Phys. Rev.* **109**, 1492 (1958).
- [24] D. Basko, I. Aleiner, and B. Altshuler, *Annals of Physics* **321**, 1126 (2006).
- [25] R. Nandkishore and D. A. Huse, *Annual Review of Condensed Matter Physics* **6**, 15 (2015).
- [26] D. A. Abanin, E. Altman, I. Bloch, and M. Serbyn, *Rev. Mod. Phys.* **91**, 021001 (2019).
- [27] P. Sierant, M. Lewenstein, A. Scardicchio, L. Vidmar, and J. Zakrzewski, Many-body localization in the age of classical computing (2024), [arXiv:2403.07111](https://arxiv.org/abs/2403.07111) [cond-mat.dis-nn].
- [28] J. Eisert, M. Cramer, and M. B. Plenio, *Rev. Mod. Phys.* **82**, 277 (2010).
- [29] C. Cao, J. Xue, N. Shannon, and R. Joynt, *Phys. Rev. Res.* **3**, 013092 (2021).
- [30] S. Liu, S.-X. Zhang, C.-Y. Hsieh, S. Zhang, and H. Yao, *Phys. Rev. B* **107**, 024204 (2023).
- [31] J. Tangpanitanon, S. Thanasilp, N. Dangniam, M.-A. Lemonde, and D. G. Angelakis, *Phys. Rev. Res.* **2**, 043364 (2020).
- [32] K. Su and M. J. Lawler, *Phys. Rev. B* **106**, 214310 (2022).
- [33] D. Zhu, S. Johri, N. H. Nguyen, C. H. Alderete, K. A. Landsman, N. M. Linke, C. Monroe, and A. Y. Matsuura, *Phys. Rev. A* **103**, 032606 (2021).
- [34] O. Shtanko, D. S. Wang, H. Zhang, N. Harle, A. Seif, R. Movassagh, and Z. Mineev, Uncovering local integrability in quantum many-body dynamics (2023), [arXiv:2307.07552](https://arxiv.org/abs/2307.07552) [quant-ph].
- [35] P. Ponte, Z. Papić, F. m. c. Huvneers, and D. A. Abanin, *Phys. Rev. Lett.* **114**, 140401 (2015).
- [36] A. Lazarides, A. Das, and R. Moessner, *Phys. Rev. Lett.* **115**, 030402 (2015).
- [37] D. A. Abanin, W. De Roeck, and F. Huvneers, *Annals of Physics* **372**, 1 (2016).
- [38] D. R. Hartree, *Mathematical Proceedings of the Cambridge Philosophical Society* **24**, 89–110 (1928).
- [39] D. R. Hartree, *Mathematical Proceedings of the Cambridge Philosophical Society* **24**, 111–132 (1928).
- [40] F. Verstraete, V. Murg, and J. Cirac, *Advances in Physics* **57**, 143 (2008).
- [41] U. Schollwöck, *Annals of Physics* **326**, 96 (2011), january 2011 Special Issue.
- [42] J. M. Renes, R. Blume-Kohout, A. J. Scott, and C. M. Caves, *Journal of Mathematical Physics* **45**, 2171 (2004).
- [43] D. Gross, K. Audenaert, and J. Eisert, *Journal of Mathematical Physics* **48**, 10.1063/1.2716992 (2007), 052104.
- [44] C. Dankert, R. Cleve, J. Emerson, and E. Livine, *Phys. Rev. A* **80**, 012304 (2009).
- [45] A. D. Luca and A. Scardicchio, *Europhysics Letters* **101**, 37003 (2013).
- [46] D. J. Luitz, X. Plat, F. Alet, and N. Laflorencie, *Phys. Rev. B* **91**, 155145 (2015).
- [47] S. Sim, P. D. Johnson, and A. Aspuru-Guzik, *Advanced Quantum Technologies* **2**, 1900070 (2019).
- [48] A. W. Harrow, The church of the symmetric subspace (2013), [arXiv:1308.6595](https://arxiv.org/abs/1308.6595) [quant-ph].
- [49] A. Pal and D. A. Huse, *Phys. Rev. B* **82**, 174411 (2010).
- [50] L. Leone, S. F. E. Oliviero, and A. Hamma, *Phys. Rev. Lett.* **128**, 050402 (2022).
- [51] S. F. E. Oliviero, L. Leone, and A. Hamma, *Phys. Rev. A* **106**, 042426 (2022).
- [52] D. Rattacaso, L. Leone, S. F. E. Oliviero, and A. Hamma, *Phys. Rev. A* **108**, 042407 (2023).
- [53] N. P. Breuckmann and J. N. Eberhardt, *PRX Quantum* **2**, 040101 (2021).
- [54] D. N. Page, *Phys. Rev. Lett.* **71**, 1291 (1993).
- [55] S. K. Foong and S. Kanno, *Phys. Rev. Lett.* **72**, 1148 (1994).
- [56] M. B. Hastings, *Journal of Statistical Mechanics: Theory*

- and *Experiment* **2007**, P08024 (2007).
- [57] S. Aubry and G. André, *Ann. Israel Phys. Soc* **3**, 18 (1980).
- [58] P. Jordan and E. Wigner, *Zeitschrift für Physik* **47**, 631 (1928).
- [59] S. Iyer, V. Oганesyan, G. Refael, and D. A. Huse, *Phys. Rev. B* **87**, 134202 (2013).
- [60] R. Orús, *Nature Reviews Physics* **1**, 538 (2019).
- [61] M. Cerezo, M. Larocca, D. García-Martín, N. L. Diaz, P. Braccia, E. Fontana, M. S. Rudolph, P. Bermejo, A. Ijaz, S. Thanasilp, E. R. Anschuetz, and Z. Holmes, Does provable absence of barren plateaus imply classical simulability? or, why we need to rethink variational quantum computing (2023), [arXiv:2312.09121 \[quant-ph\]](https://arxiv.org/abs/2312.09121).
- [62] G. Vidal, *Phys. Rev. Lett.* **93**, 040502 (2004).
- [63] C. Zoufal, A. Lucchi, and S. Woerner, *npj Quantum Information* **5**, 103 (2019).
- [64] X. Mi, P. Roushan, C. Quintana, S. Mandrà, J. Marshall, C. Neill, F. Arute, K. Arya, J. Atalaya, R. Babush, J. C. Bardin, R. Barends, J. Basso, A. Bengtsson, S. Boixo, A. Bourassa, M. Broughton, B. B. Buckley, D. A. Buell, B. Burkett, N. Bushnell, Z. Chen, B. Chiaro, R. Collins, W. Courtney, S. Demura, A. R. Derk, A. Dunsworth, D. Eppens, C. Erickson, E. Farhi, A. G. Fowler, B. Foxen, C. Gidney, M. Giustina, J. A. Gross, M. P. Harrigan, S. D. Harrington, J. Hilton, A. Ho, S. Hong, T. Huang, W. J. Huggins, L. B. Ioffe, S. V. Isakov, E. Jeffrey, Z. Jiang, C. Jones, D. Kafri, J. Kelly, S. Kim, A. Kitaev, P. V. Klimov, A. N. Korotkov, F. Kostritsa, D. Landhuis, P. Laptev, E. Lucero, O. Martin, J. R. McClean, T. McCourt, M. McEwen, A. Megrant, K. C. Miao, M. Mohseni, S. Montazeri, W. Mruczkiewicz, J. Mutus, O. Naaman, M. Neeley, M. Newman, M. Y. Niu, T. E. O'Brien, A. Opremcak, E. Ostby, B. Pato, A. Petukhov, N. Redd, N. C. Rubin, D. Sank, K. J. Satzinger, V. Shvarts, D. Strain, M. Szalay, M. D. Trevithick, B. Villalonga, T. White, Z. J. Yao, P. Yeh, A. Zalcman, H. Neven, I. Aleiner, K. Kechedzhi, V. Smelyanskiy, and Y. Chen, *Science* **374**, 1479 (2021).
- [65] Y. Yu, C. Cao, C. Dewey, X.-B. Wang, N. Shannon, and R. Joynt, *Phys. Rev. Res.* **4**, 023249 (2022).
- [66] Z.-H. Sun, Y.-Y. Wang, J. Cui, and H. Fan, *New Journal of Physics* **25**, 013015 (2023).
- [67] X. Yuan, S. Endo, Q. Zhao, Y. Li, and S. C. Benjamin, *Quantum* **3**, 191 (2019).
- [68] M. Benedetti, M. Fiorentini, and M. Lubasch, *Phys. Rev. Res.* **3**, 033083 (2021).
- [69] S.-J. Ran, *Phys. Rev. A* **101**, 032310 (2020).
- [70] M. S. Rudolph, J. Chen, J. Miller, A. Acharya, and A. Perdomo-Ortiz, *Quantum Science and Technology* **9**, 015012 (2023).
- [71] D. Malz, G. Styliaris, Z.-Y. Wei, and J. I. Cirac, *Phys. Rev. Lett.* **132**, 040404 (2024).
- [72] C. Cao, H. Yano, and Y. O. Nakagawa, *Phys. Rev. Res.* **6**, 013205 (2024).
- [73] L. Mineh and A. Montanaro, *Quantum Science and Technology* **8**, 035012 (2023).
- [74] C.-Y. Park, M. Kang, and J. Huh, Hardware-efficient ansatz without barren plateaus in any depth (2024), [arXiv:2403.04844 \[quant-ph\]](https://arxiv.org/abs/2403.04844).
- [75] R. R. Tucci, An introduction to cartan's kak decomposition for qc programmers (2005), [arXiv:quant-ph/0507171 \[quant-ph\]](https://arxiv.org/abs/quant-ph/0507171).
- [76] A. Y. Kitaev, *Russian Mathematical Surveys* **52**, 1191 (1997).
- [77] S. Datta, S. Howard, and D. Cochran, *Linear Algebra and Its Applications* **437**, 2455 (2012).
- [78] R. N. Youngworth, B. B. Gallagher, and B. L. Stamper, in *Optical Manufacturing and Testing VI*, Vol. 5869, edited by H. P. Stahl, International Society for Optics and Photonics (SPIE, 2005) p. 58690U.